Supporting Information

for

Enzyme-assembled gel monolithic microreactor for continuous flow asymmetric synthesis of aryl alcohols

Qiang Chen,[a] Yuchao An,[a] Mingjian Feng,[a] Jincheng Li,[b] Yanjie Li,[c] Feifei Tong,[b] Ge Qu,[b] Zhoutong Sun,[b] Guangsheng Luo,[a] and Yujun Wang*[a]

[a]   Q. Chen, Y. An, M. Feng, Prof. Dr. G. Luo, Prof. Dr. Y. Wang
      The State Key Lab of Chemical Engineering, Department of Chemical Engineering,
      Tsinghua University, Beijing 100084, China
      E-mail: wangyujun@mail.tsinghua.edu.cn

[b]   J. Li, F. Tong, Dr. G. Qu, Prof. Dr. Z. Sun
      Tianjin Institute of Industrial Biotechnology, Chinese Academy of Sciences,
      Tianjin 300308, China

[c]   Y. Li
      Technology Center for Protein Sciences, School of Life Sciences,
      Tsinghua University, Beijing 100084, China

Abstract: The green, efficient, and sustainable flow synthesis of intermediate chiral aryl alcohols is critical for continuous drug-manufacturing. Enzyme immobilization endows flow biocatalysis with higher application potential, however, conventional methods are limited by cumbersome operations, a trade-off between activity and stability, and low loading due to the required support. Here, we demonstrated the microfluidic induction of alcohol dehydrogenase to form enzyme-assembled gels (EAG) in a microreactor, with controllable mechanical properties and porous architecture. Six chiral aryl alcohols were successfully synthesized by using this approach in flow asymmetric reduction. Moreover, the support-free EAG was capable of in situ flow immobilization and reversible de-immobilization without reactor disassembly. The EAG monolithic microreactor presented an excellent space-time yield of 88.05 g L^{-1} h^{-1} and a high total turnover number of 62600 after 100 h of operation (over 1300 reactor volumes), highlighting its high activity and stability.

Table of Contents

1. Experimental Section

1.1 Materials.

1.2 Fabrication of chip reactor MC-MCR and SC-MCR.

1.3 Expression and purification of proteins.

1.4 Preparation of E_Hmtz and EAGs.

1.5 Cryo-EM images collection.

1.6 In situ preparation of EAG monolithic microreactor.

1.7 Dynamic light scattering (DLS).

1.8 Rheological tests.

1.9 Characterizations.

1.10 Biocatalytic activity assay.

1.11 Comparison of three reaction modes: flow-gel, batch-gel, and batch-E.

2. Supplementary Figures

Figure S1-Figure S14.

3. Supplementary Tables

Table S1-Table S4.

4. Supplementary Note

Supplementary Note 1.

5. Reference Section

Reference 1 to Reference 6.

Experimental Section

Materials

1-phenoxy-2-propanone (**1b**, 98%), 4-fluorophenylacetone (**1c**, 97%), 1-phenyl-3-butanone (**1d**, 98%), and 3-methyl-1H-1,2,4-trizole (Hmtz, 98%) were purchased from Shanghai Bide Pharmatech Ltd. Acetophenone (**1a**, 99%), 2,2,2-trifluoro-1-phenyl-1-ethanone (**1f**, 98%), ethyl 2-oxo-4-phenylbutyrat (**1e**, 97%), *β*-nicotinamide adenine dinucleotide phosphate (NADP$^+$, 98%), and isopropyl alcohol (IPA, 99.9%) were purchased from Energy Chemical Technology (Shanghai) Co., Ltd. Magnesium nitrate hexahydrate (≥99%) was purchased from Sinopharm Chemical Reagent Co., Ltd. All reagents and chemicals were purchased from commercial sources and used without further purification. Quantifoil (Cu R1.2/1.3, 300 mesh) was acquired from Beijing Zhongjing Keyi Technology Co., Ltd.

Fabrication of chip reactor MC-MCR and SC-MCR

An LSmicro2020 CNC engraving machine was used to engrave the meandering or straight channel on a transparent polymethyl methacrylate (PMMA) plate with a processing speed of 22000 rpm. The feed speed was 35 mm/min with a processing time of approximately 79 min; the carving process was completed with a milling cutter of the LSmicro series (blade diameters of 200 and 500 μm). The screw and interface sinks on the reverse side of the structural plate were machined at a processing speed of 22000 rpm for approximately 39 min, for which a milling cutter with a 2000 μm blade diameter (LSmicro series) was used. M4 taps were tapped to form threads in the screw holes of the base plate, while 1/4-28UNF was used to tap the sink holes of the upper cover injection holes to form threads. The two plates were cleaned twice with ultrasonic pure water to remove impurities and burrs and then dried at 75 °C for 30 min in a vacuum drying oven. Finally, the chips were formed by assembling plates engraved with microchannels, where the silicone sheets were sandwiched between the plates for sealing. Excluding the volume occupied by quartz wool, the total volumes of the MC-MCR and SC-MCR were both 80 μL.

Expression and purification of proteins

Escherichia coli BL21 (DE3, Novagen) cells carrying the recombinant plasmid were cultivated in 5 mL LB medium containing kanamycin (50 ug/mL) for 8~10 h in a 220-rpm shaker at 37°C. The culture was then inoculated into 100 mL of TB medium containing 50 ug/mL kanamycin and grown

at 37°C for about 3 h. Addition of isopropyl β-D-1thiogalactopyranoside (IPTG, final concentration of 0.2 mM) was induced by when OD_{600} reached 0.4~0.6, and then allowed to grow for additional 15 h at 20°C. After centrifugation at 4000 rpm for 8 min at 4°C, the bacterial pellet was resuspended in PBS (1 g:10 mL) after wash. The cells were lysed by sonication for 15 min and the supernatant was collected by centrifugation for 10 min at 4°C.

Protein purification was performed at 23°C using an AKTA Purifier system (Unicorn software) equipped with an affinity chromatography (HisTrap-FF (GE, USA)). Pre-equilibration was carried out with 50 mL of 20 mM phosphate buffer (containing 20 mM imidazole, 0.5 M NaCl, 5% glycerin, pH 7.4). Crude sample was loaded with a flow rate of 2.0~3.0 mL/min. After rinsing the 50 mL equilibrium buffe, the flow rate was increased to 5 mL/min and flush until the UV baseline was stable, at which time most of the impurity proteins had flowed into the waste. Then a 30-min gradient elution was performed at a flow rate of 3 mL/min, with imidazole concentration increasing from 20 mM to 500 mM and NaCl concentration decreasing from 0.5 M to 0. The purified protein was collected and desalted through a desalting column (Model HiPrep 26/10, GE) against 20 mM phosphate buffer (containing 0.1 M NaCl, 5% glycerin, pH 7.4).

The alcohol dehydrogenase used in this work was a mutant from *Thermodehydrogenase brockii*, which is a promising catalyst for a series of biocatalytic applications.[1-3] Not only pure ADH but also crude enzyme powder is capable of generating EAG.

Preparation of E_Hmtz and EAGs

Unless otherwise specified, 0.6 mg/mL TbSADH was mixed with 31.2 mg/mL Hmtz in a 10 mL phosphate buffer solution (PBS, 50 mM, pH 7.4) at room temperature and stirred at 200 rpm for 10 min (Δt) of pregelation. Then, 1 mL of PBS (for E_Hmtz) or 1 mL of PBS containing 5–100 mM magnesium nitrate hexahydrate (for EAGs) was added and mixed for 2 h ($t(G)$) of gelation. Unless otherwise noted, a magnesium ion concentration of 50 mM was used by default for EAG synthesis. The obtained solid gel was centrifuged (4000 rpm, 5 min) and washed thrice with Milli-Q water. Lyophilized samples were obtained by freezing the gel using liquid nitrogen and then transferring it to a freeze dryer for 12 h.

Cryo-EM images collection

After 5 min of gelation, 4 μl of the solution was quickly applied to a hydrophilized Quantifoil (Cu R1.2/1.3, 300 mesh carbon grids). The grid was blotted for 2.5 s (8°C, 100% humidity, and 15 s of waiting time) with filter paper to remove excess sample and then plunge-frozen in liquid ethane

(-180 °C) cooled by liquid nitrogen using a Vitrobot Mark IV (FEI). Cryo-EM data were collected using an FEI Falcon II direct electron detector on a Tecnai Arctica (FEI) microscope equipped with a Gatan Orius SC200B (830) CCD (operated at 200 kV acceleration voltage).

In situ preparation of EAG monolithic microreactor

As shown in Figure 2a, 1.2 mg/mL TbSADH PBS and 62.4 mg/mL Hmtz PBS are pumped at a flowrate of Q_1 and mixed with a micromixer. After being passed through a delay loop with a length of L_1, the fluid was mixed with a 20–80 mM magnesium ion solution (unless otherwise noted, the magnesium ion concentration was 50 mM) with a flowrate of Q_2 through another micromixer. After the mixed solution passed through another delay loop of length L_2, it entered the chip microchannel to generate the EAG monolith. The total flow Q(F) was controlled by adjusting Q_1 and Q_2 as follows:

$$Q(\text{F}) = 2Q_1 + Q_2 \; ; \quad Q_1 : Q_2 = 10 : 1$$

Δt and $t(\text{G})$ were controlled by changing the lengths of delay loops, as follows:

$$\Delta t = \frac{L_1}{2Q_1} \; ; \; t(\text{G}) = \frac{L_2}{2Q_1 + Q_2}$$

Typically, Δt=10 min and $t(\text{G})$=120 min.

Dynamic light scattering (DLS)

A time-dependent increase in hydrodynamic diameter upon gelation at 25℃ was recorded by dynamic light scattering (DLS) using a Nano-Series ZetaSizer (Zetasizer Nano ZS90, Malvern Instruments) equipped with a He-Ne laser (633 nm). Light scattering was detected at 173 Â°. The growth of the EAG was measured immediately after the enzyme solution was mixed with the Hmtz solution in a UV-cuvette; each solution was allowed to reach a constant temperature of 25 °C prior to the test.[4] The average hydrodynamic diameter (Z-average) of the EAG particles calculated from autocorrelated light intensity using ZetaSizer software was recorded over a period of 40 min or more, with individual measurements taken every 10 s. The increase in the average hydrodynamic diameter within the first 3 min was linearly fitted and used to demonstrate the effect of Hmtz/E stoichiometry on hydrogelation, while the average diameter at 40 min was used to evaluate the effect of enzyme concentration. To determine the EAG growth curves at different magnesium ion concentrations, different concentrations of magnesium ion solutions were rapidly added to the UV cuvette 10 min after Hmtz and E were mixed. The change in the diameter was monitored for 120 min. A second- or third-order polynomial fit was performed on the measured diameter change to obtain a correlation between the EAG diameter and gelation time.

Rheological tests

Rheological tests were performed on 500 µL of hydrogels after 40 min of induced gelation (Anton Par MCR301, PP25 25 mm parallel steel plates, Austria) with a measuring gap of 1 mm. The storage (G') and loss (G") moduli were measured as a function of time (s) at a constant frequency of 1 Hz and strain of 0.1%. Periodic strain sweeps were performed at 5 step strain sweeps of 20% strain (200 s), followed by a 400 s recovery period (0.1% strain), where the frequency was constant at 1 Hz. To determine the effect of temperature, pH, and IPA concentration on the modulus, after one time period, the temperature of the sample chamber was changed (or the samples were replaced with different pH and IPA concentrations) and the subsequent time period test was conducted.

Characterizations

The porous structure of the EAG was characterized by using scanning electron microscopy (SEM, JEOL 7900 F, Japan). Fourier transform infrared (FTIR) spectra were recorded on a PerkinElmer Frontier spectrometer. Online UV monitoring was performed by connecting the HD-3000 with an 80 µl flow cell (in series at the reactor outlet). N_2 adsorption and desorption data were obtained using a Tristar II 3020 (Micromeritics, USA) surface area and pore size analyzer. Small-angle X-ray scattering (SAXS) was performed using a Bruker Nanostar with a Vantec-2000 2D detector. Thermo Scientific K-Alpha with 1486.6 eV Al Kα rays as the excitation source was used to obtain the X-ray photoelectron spectroscopy (XPS) of various EAGs. Powder X-ray diffraction (PXRD) patterns were recorded on a Rigaku Ultima IV (Japan) X-ray diffractometer with a Cu Kα anode (λ=1.5418 nm) at 40 kV and 40 mA. Raman spectra were measured on a HORIBA Scientific LabRAM HR Evolution instrument with a 514 nm laser.

Biocatalytic activity assay

For batch reactions, unless otherwise specified, the default reaction solution used to characterize activity was 1 mL of PBS (50 mM, pH 7.4) containing 5 mM **1a**, 1 mM $NADP^+$, 10% IPA and 6.5 µM ADH. The reaction was shaken for 10 min at 600 rpm at 30 °C. After reaching the reaction time, 20 µL of the solution was sampled and the product and remaining substrate in the sample were extracted with 200 µL of ethyl acetate by vortexing. The upper organic phase was removed and the solute was replaced with isopropanol. The conversion rate and chiral selectivity were determined by HPLC analysis. Agilent 1260 (Agilent Technologies Singapore (International) Pte. Ltd.,

Singapore) equipped with a Chiralcel OD-H column (4.6 mm × 250 mm, 5 μm, Diacel) and an ultraviolet detector G1314B was used for the HPLC analysis, which was performed at 30 °C with a detection wavelength of 220 nm using *n*-hexane:isopropanol (92:8 or 75:25, v/v) as the eluent at a flowrate of 1.0 mL/min (Table S6). For the flow reactions, unless otherwise specified, PBS (50 mM, pH 7.4) containing 5 mM **1a**, 1 mM $NADP^+$, and 10% IPA was continuously pumped into the EAG monolithic microreactor. The reaction liquid was collected at the reactor outlet and 20 μL of the solution was sampled to determine the conversion and selectivity. Unless otherwise specified, the reaction conditions for **1b–1f** were the same as those mentioned earlier.

Comparison of the three reaction modes: flow-gel, batch-gel, and batch-E

For the flow reaction involving EAG, the flowrate was 20 μL/min and the ADH content of the EAG monolith was 9.5 mg. The pumped-in reaction solution contained 50 mM **1a**, 1 mM $NADP^+$ and 10% IPA. The STY of the flow mode was calculated from the conversion measured at the outlet solution under the above conditions. t_{90} was determined by changing the flowrate to obtain conversions at different residence times. For the batch reaction, the volume of the reaction solution was 120 mL (equivalent to the outlet volume of a 100-h run in flow mode), containing 50 mM substrate **1a**, 1 mM $NADP^+$, 10% IPA, and 9.5 mg ADH in free enzyme or EAG, with stirring at 300 rpm. The solution was sampled every 1 h to measure the conversion and determine t_{90}. The STY of batch mode was calculated based on the data once the conversion rate reached 85%. The reaction temperature for the three modes was 25 °C.
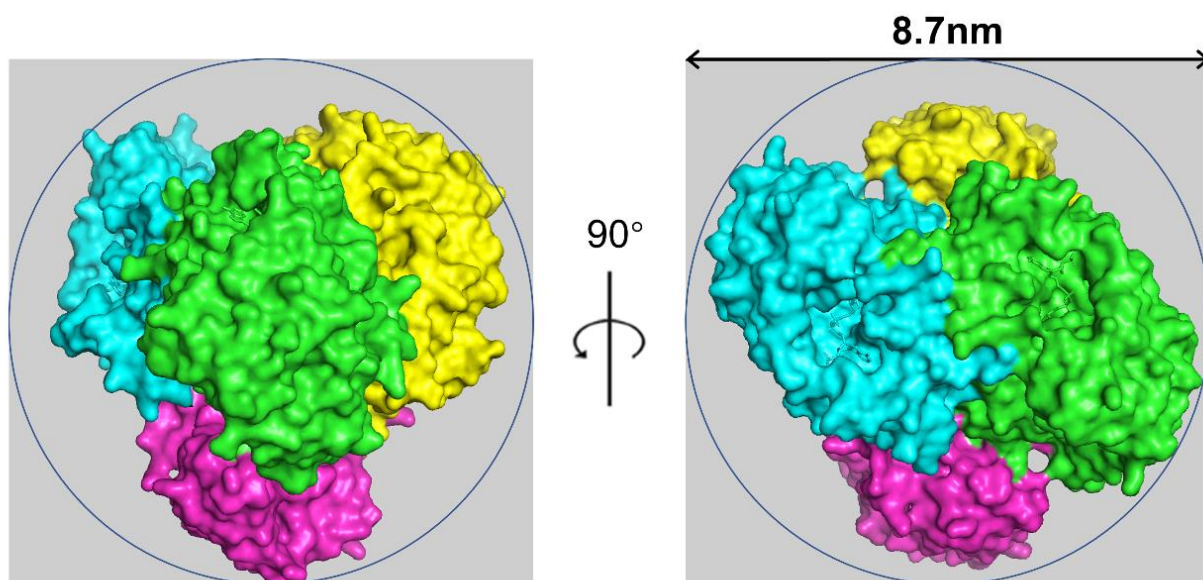
Supplementary Figures

Figure S1. Three-dimensional surface map of TbSADH with a diameter of about 8.7 nm. Four subunits were given different colors.
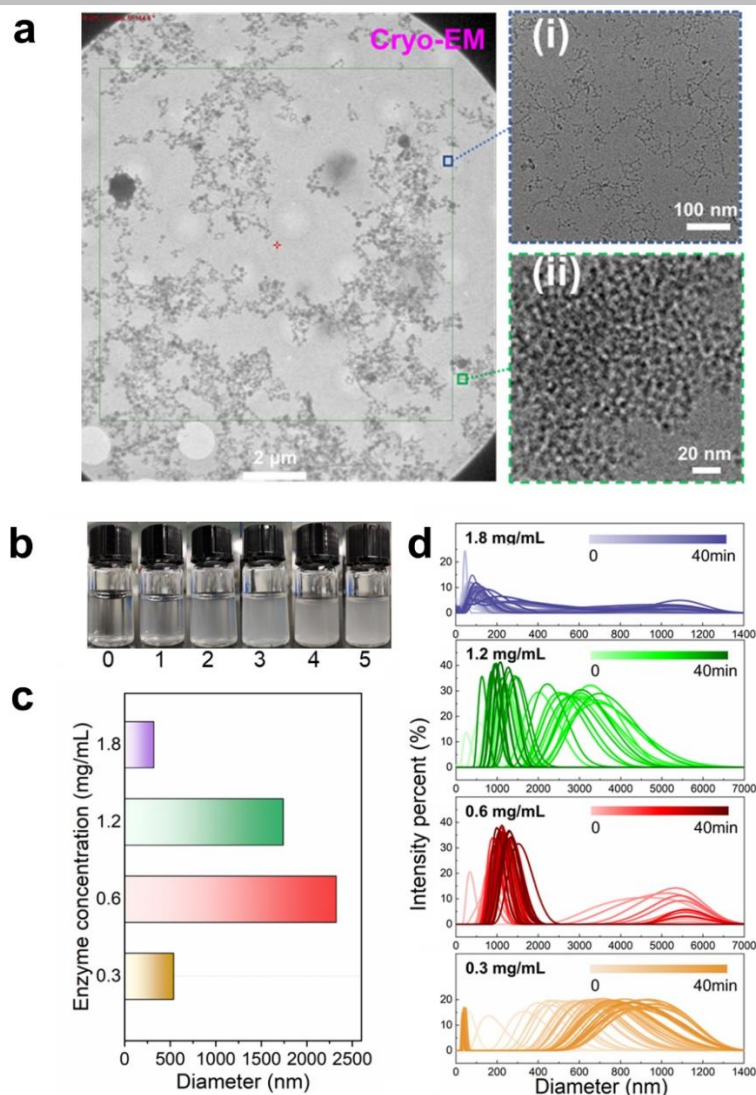
Figure S2. (a) Cryo-EM images at 5 min of gelation: (i) a magnified observation of the site where the EAG had not yet formed; (ii) the EAG edge. (b) Optical images of gelation from 0 to 5 min. (c) Comparison of EAG size at various ADH concentrations at 40 min of gelation. (d) Time evolution of EAG size distribution at various ADH concentrations. Unless otherwise specified, the concentration of ADH was 0.6 mg/mL, Hmtz:E=52:1, and Δt=10 min for the addition of 50 mM Mg^{2+}. Interestingly, in contrast to the gradual increase in size at low ADH concentrations (0.3 mg/mL), in the case of higher concentrations, a portion of the EAG initially grew rapidly to a large particle size, which then split to become consistent with the smaller size of the remaining EAG after 30 min. This may be attributed to uneven initial mixing at excessively high ADH concentrations, implying the reversibility of EAG formation in terms of splitting and integration. After 40 min, the size distribution achieved improved uniformity, while largest particle size was formed at 0.6 mg/mL. In contrast, more size distributions existed around 10 nm at 40 min in conjunction with a low ADH concentration, indicating that more ADH was not involved in EAG formation because of the small gelation driving force. However, an excessively high concentration was shown to slow dehydration during gelation.
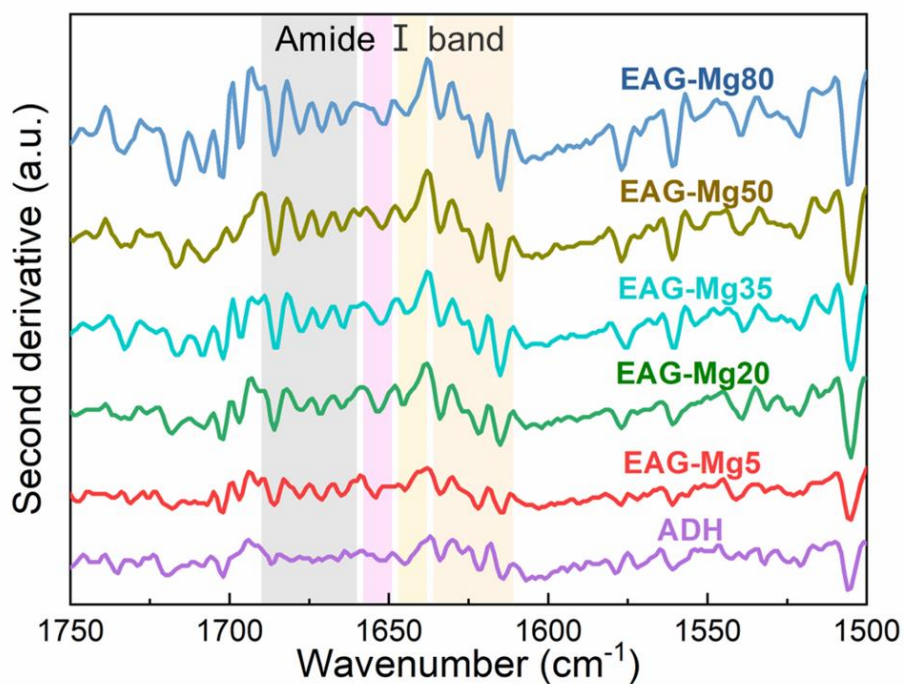
Figure S3. Second derivatives of the FTIR spectra of EAGs synthesized at different $c(Mg^{2+})$. Shadow color scheme: β-turn, gray; α-helix, pink; random coil, yellow; β-sheet, orange. The concentration of ADH was 0.6 mg/mL, Hmtz:E=52:1, and Δt=10 min for the addition of 0–80 mM Mg^{2+}.
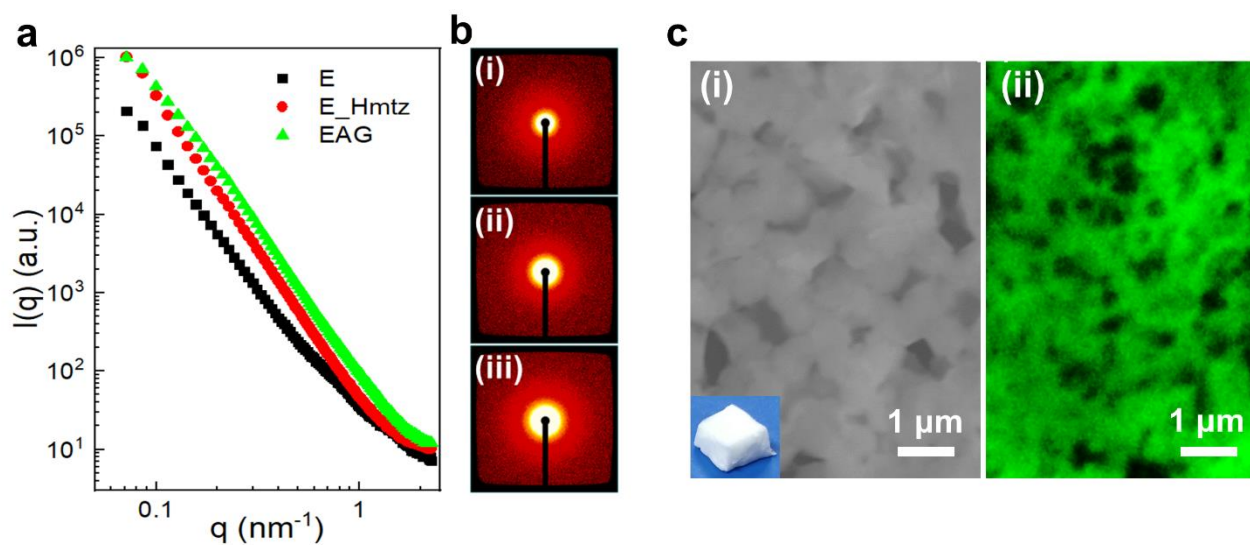
Figure S4. (a) SAXS profiles of ADH (E), gel without Mg^{2+} addition (E_Hmtz) and EAG. (b) The two-dimensional (2D) SAXS scattering patterns obtained from (i) E, (ii) E_Hmtz, and (iii) EAG. (c) Scanning electron microscope (SEM) image of EAG in lyophilized state (i), and confocal laser scanning microscopy (CLSM) image in aqueous solution (ii). The inset was the optical image of the lyophilized EAG. The concentration of ADH was 0.6 mg/mL, Hmtz:E=52:1, and Δt=10 min for the addition of 50 mM Mg^{2+}.
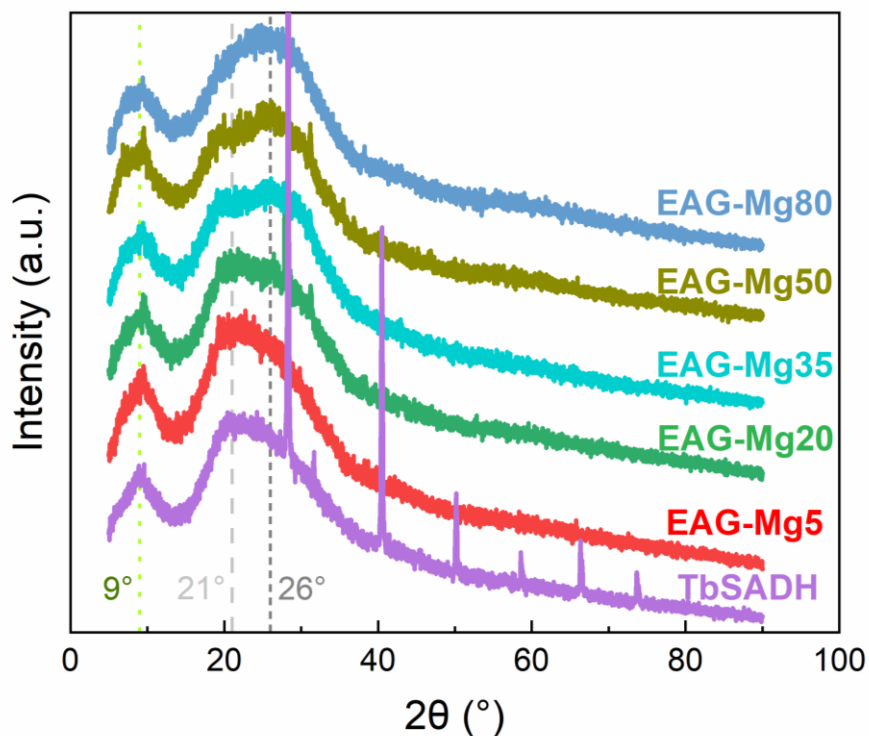
Figure S5. PXRD patterns of the freeze-dried enzyme powder and EAGs synthesized with different concentrations of magnesium ions. Large flat peaks indicate that both enzyme and EAG are amorphous. As the concentration of magnesium ions increased, the peaks at 9° did not shift, which corresponds to the characteristic diameter of the enzyme molecule of about 9.8 nm. The large flat peaks at 21° shifted to 26° with the increase of magnesium ion concentration, suggesting that magnesium ions increased the interaction between enzyme molecules, resulting in a decrease in the distance between them.
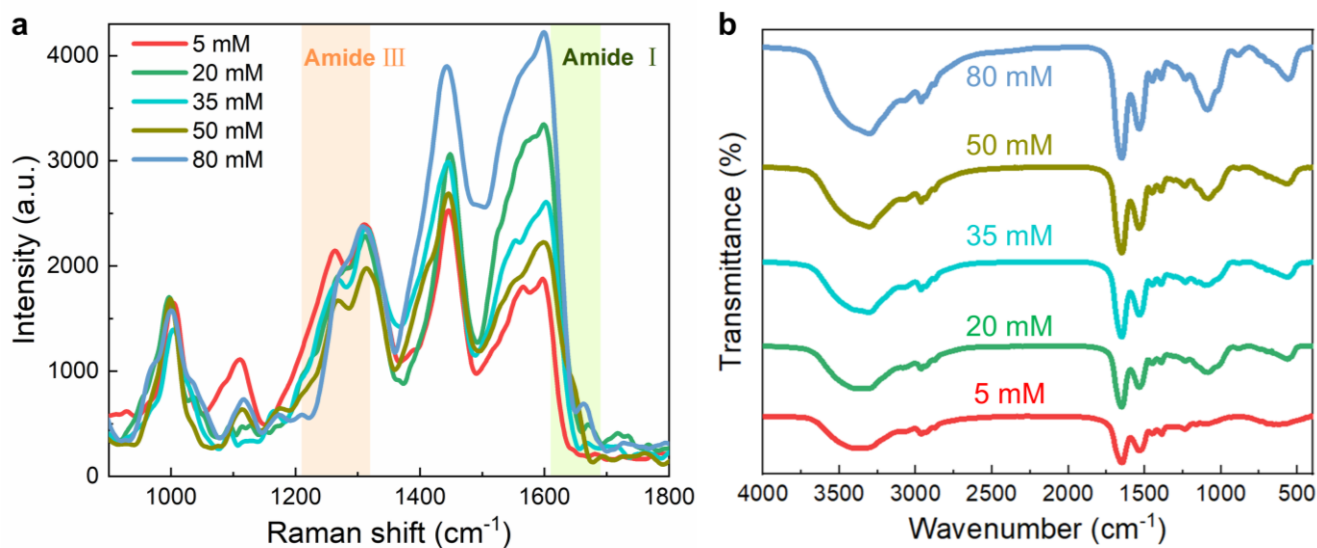
Figure S6. Raman (a) and FTIR (b) spectra of EAG synthesized with different concentrations of magnesium ions (5-80 mM). The characteristic absorption peaks of alcohol dehydrogenase at 1535 cm^{-1} and 1650 cm^{-1} in the FTIR spectrum confirmed that EAG was mainly composed of TbSADH. The main absorption peaks of the Raman spectrum did not shift, indicating that the increase of magnesium ion concentration did not cause the obvious conformational changes of protein. Raman spectrum had a stronger signal for the amide Ⅲ band (1210~1320 cm^{-1}), and FTIR had a stronger signal for the amide Ⅰ band (1610~1690 cm^{-1}).
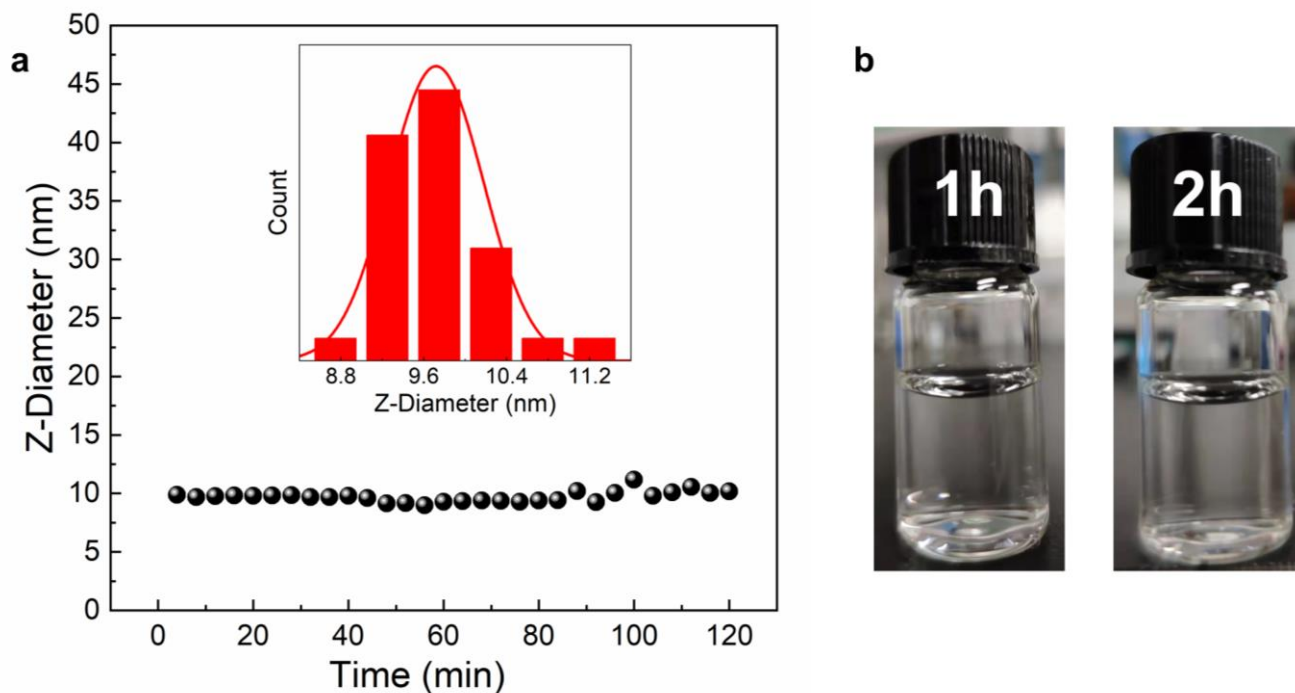
Figure S7. Growth of EAG during gelation at Hmtz: E=10:1. (a) DLS measurement of Z-average diameter every 4 min; (b) Optical photographs at 1h and 2h. At this Hmtz/E ratio, the Z-diameter did not increase and no turbidity of the solution occurred, indicating that the gelation process did not occur. The measured Z-diameter should be assigned to the hydration diameter of the protein molecule.
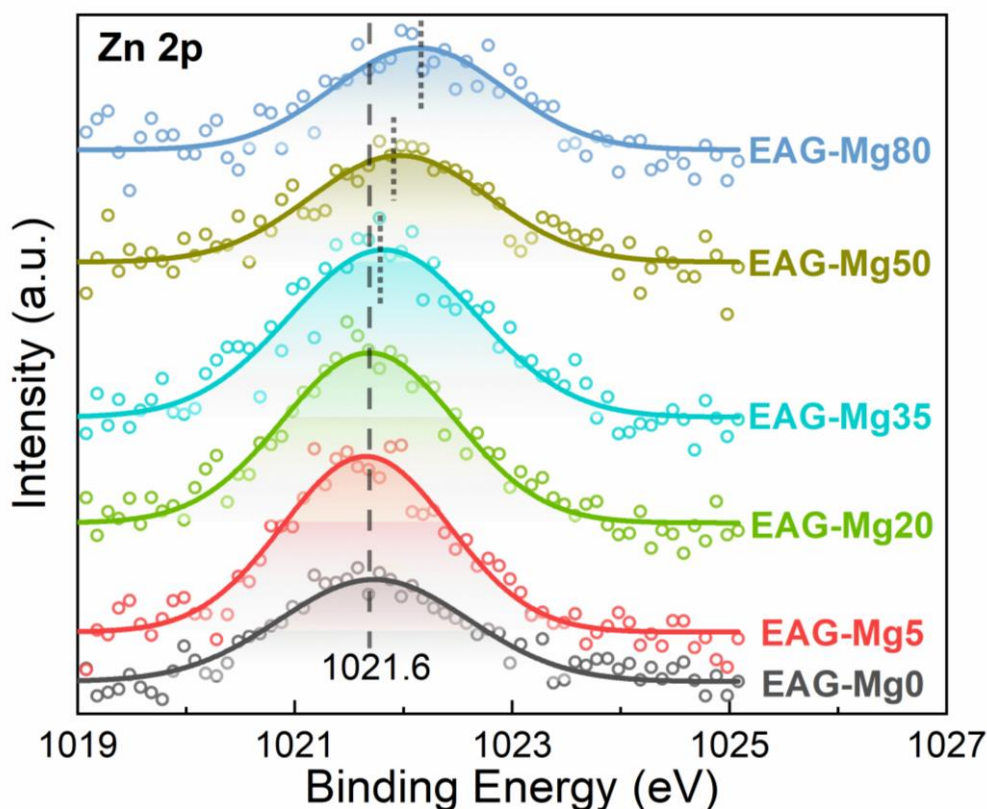
Figure S8. High-resolution Zn 2p XPS spectra of different EAGs. When the magnesium ion concentration increased from 0 to 20 mM, the binding energy of Zn 2p did not change significantly, which was 1021.6 eV. A further increase in the magnesium ion concentration resulted in a shift of the binding energy to a larger value. The binding energies at 35, 50, and 80 mM Mg^{2+} increased by 0.1, 0.2, and 0.5 eV, respectively, indicating that too high magnesium ions would reduce the original three-coordination between zinc ions and surrounding active groups, which may lead to inactivation of the active center of TbSADH.
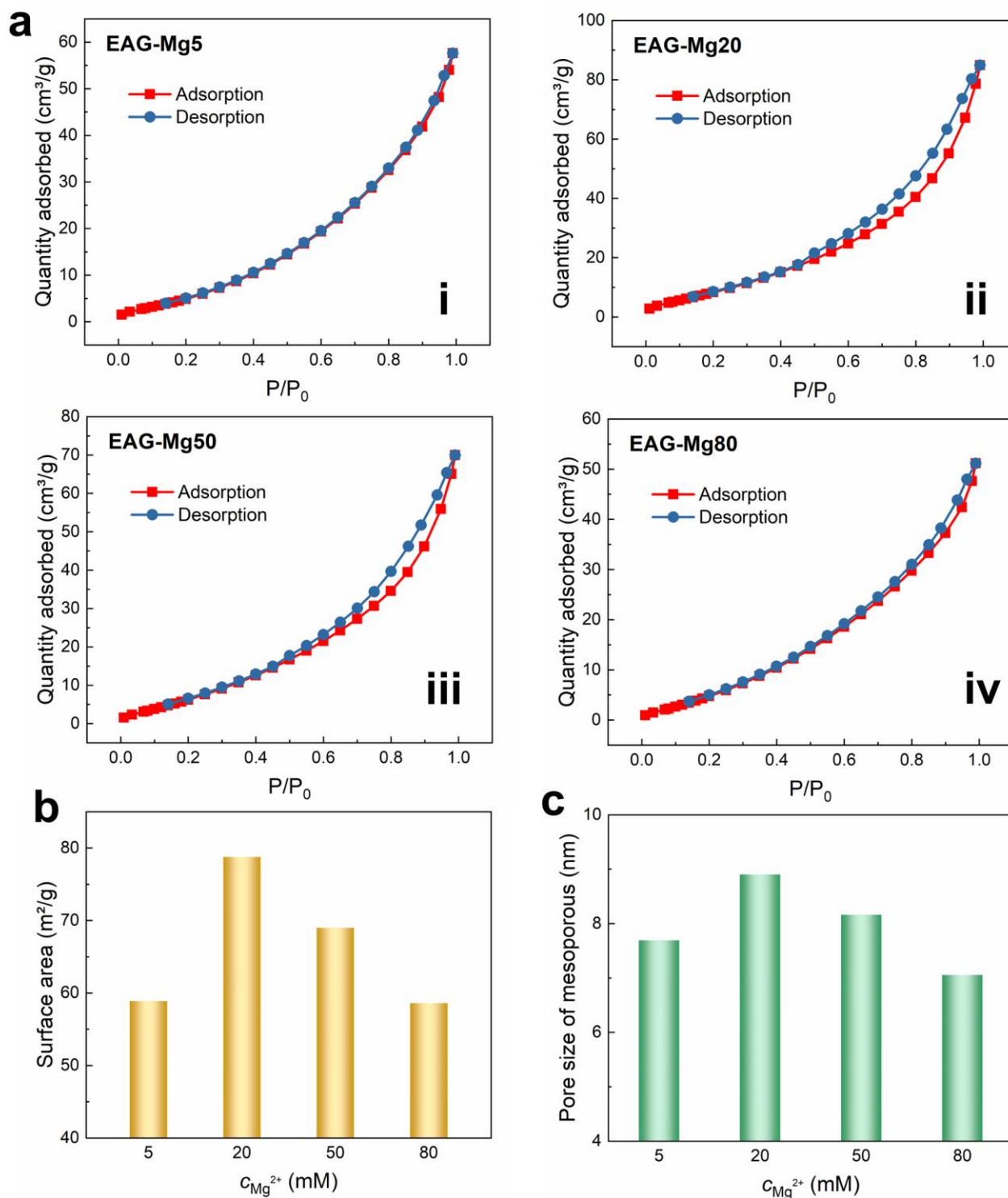
Figure S9. (a) N_2 physisorption isotherms for different EAGs. (b) Surface area of EAG synthesized with different concentrations of magnesium ions. Desorption cumulative surface area of pores between 1.7 nm and 100.0 nm diameter. Thus, the actual surface area should be larger due to many larger pores. (c) Mesoporous pore size of EAG synthesized with different concentrations of magnesium ions.

a EAG-Mg20

Fitted Equation	y = Intercept + B1*x^1 + B2*x^2
Intercept	-90.69897 ± 57.29614
B1	36.90076 ± 2.26009
B2	-0.11576 ± 0.01872
R^2	0.9603

b EAG-Mg35

Fitted Equation	y = Intercept + B1*x^1 + B2*x^2
Intercept	245.3926 ± 129.56739
B1	39.76304 ± 4.69029
B2	-0.03891 ± 0.03565
R^2	0.91763

c EAG-Mg50

Fitted Equation	y = Intercept + B1*x^1 + B2*x^2 + B3*x^3
Intercept	614.20357 ± 344.663
B1	92.47369 ± 13.31022
B2	-0.51717 ± 0.13813
B3	9.78656E-4 ± 4.06346E-4
R^2	0.69339

d EAG-Mg80

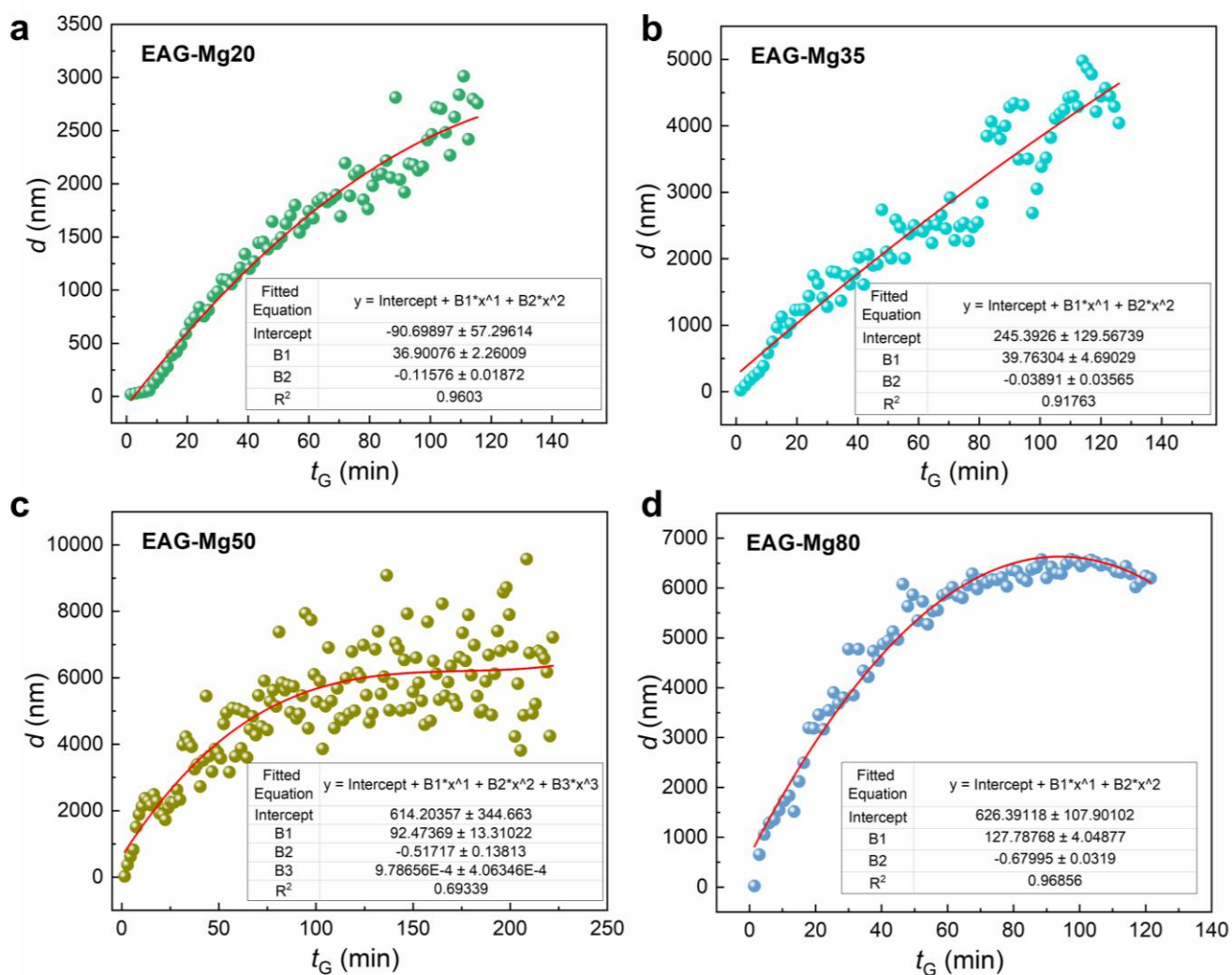| Fitted Equation	y = Intercept + B1*x^1 + B2*x^2
Intercept	626.39118 ± 107.90102
B1	127.78768 ± 4.04877
B2	-0.67995 ± 0.0319
R^2	0.96856

Figure S10. The growth curves of EAG under different magnesium ion concentrations were measured by DLS, and polynomial numerical fittings were performed. Magnesium ion concentrations: 20 mM, a; 35 mM, b; 50 mM, c; 65 mM, d. Data point was taken every 1.5 min during the DLS measurement. The abscissa is the gelation time, and the ordinate is the hydration diameter of EAG.
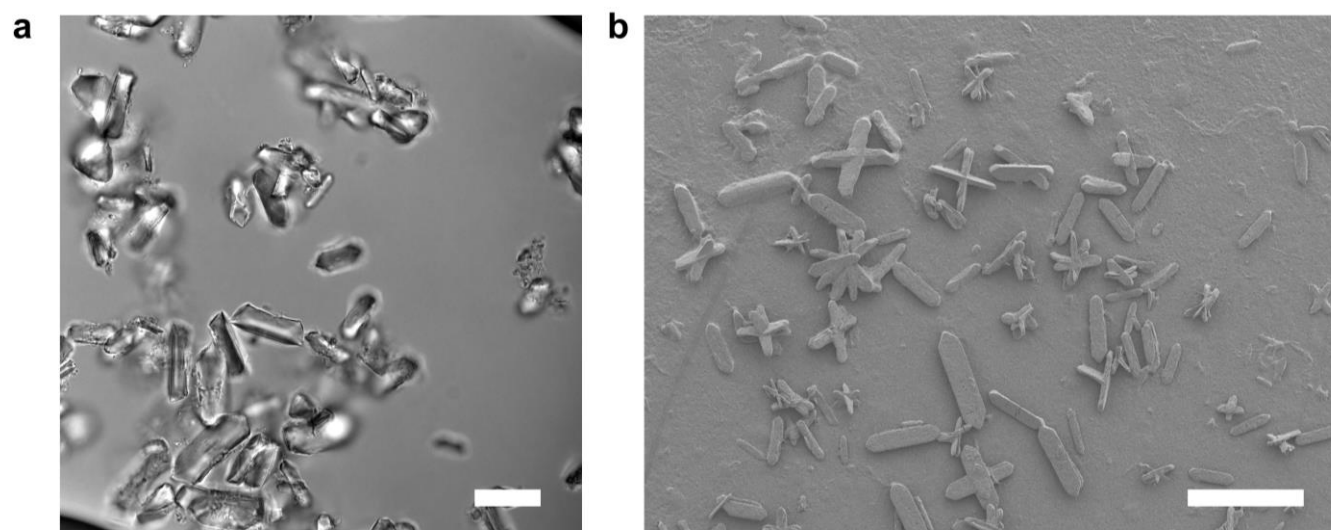
17

Figure S11. (a) In situ solution micrograph of $Mg(H_2PO_4)_2$ crystals formed after adding 100 mM magnesium ions to the phosphate buffer for 3 h, and (b) SEM image of the sample after drying. Scale bar: a, 20 µm; b, 50 µm.
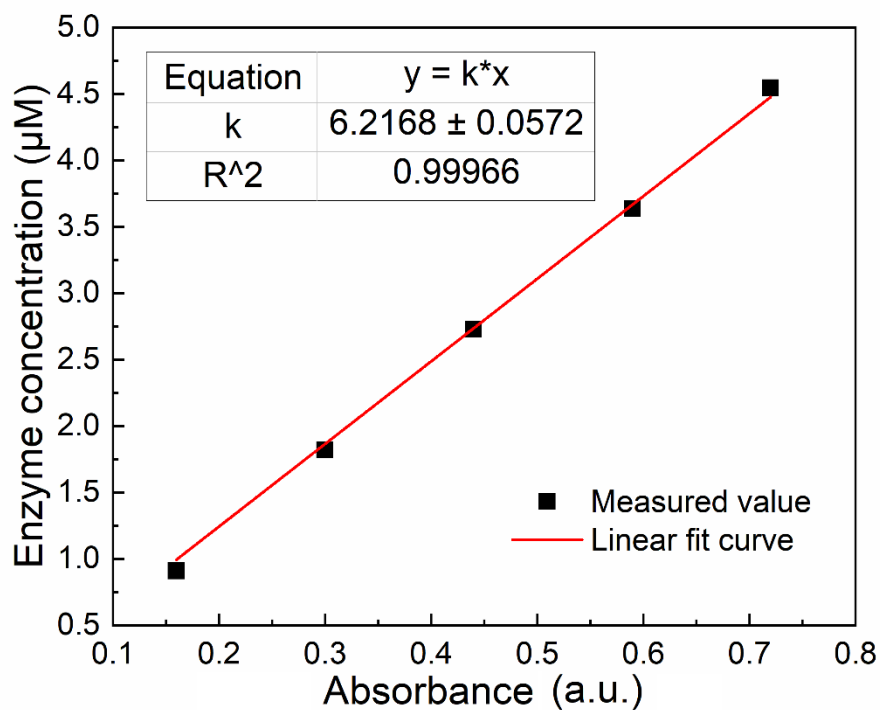
Figure S12. (a) Calibration of protein amount determined from UV absorption. Protein amount were determined by measuring the absorbance at the wavelength of 278 nm using an on-line UV detector. Enzyme solutions (0.909-4.545 μM) were selected as standards to plot the calibration curve.
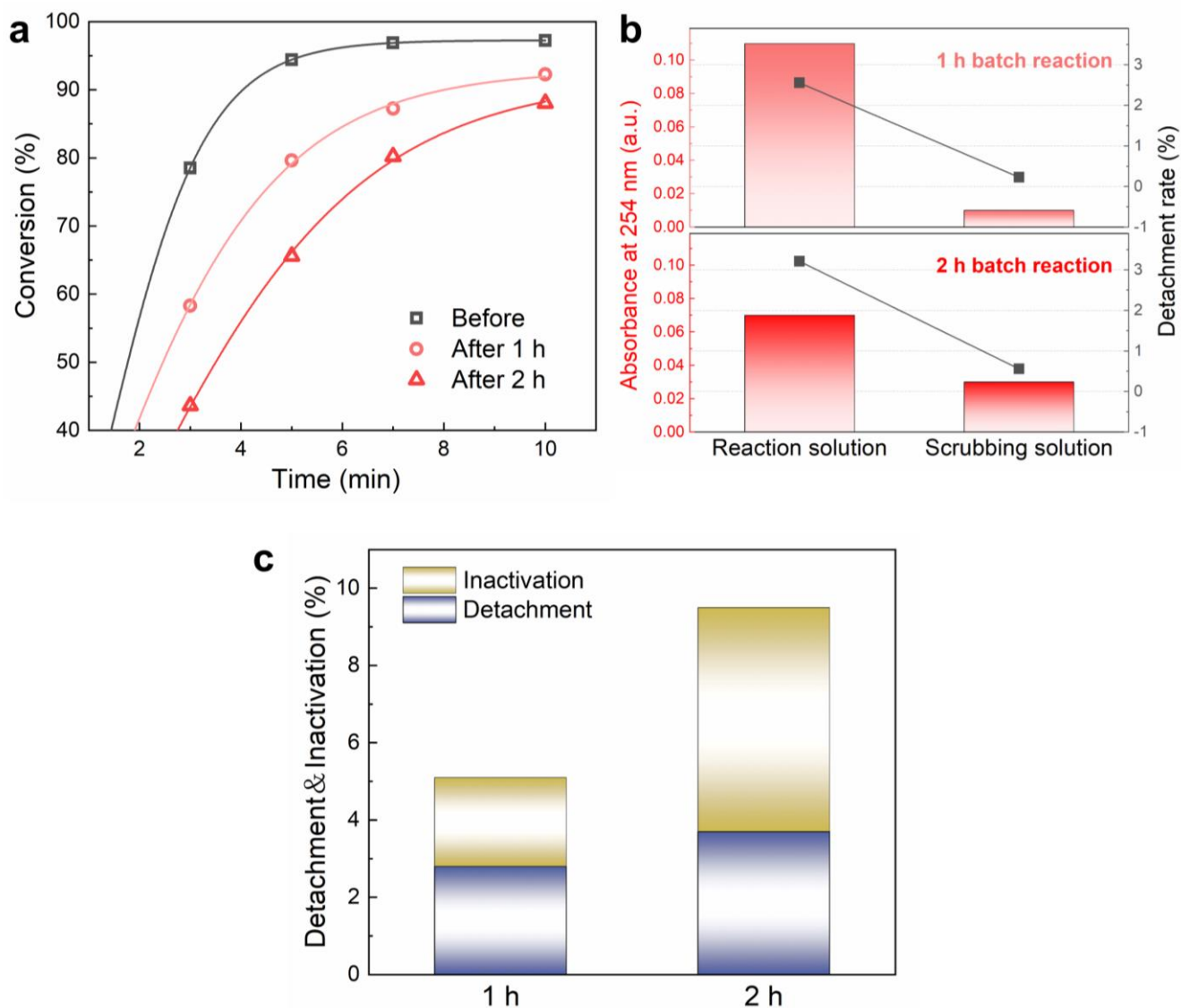
Figure S13. Inhibitory inactivation of EAG for the conversion of **1a** to **2a** in batch reaction. (a) Activity test for EAG recovered after batch reaction at 0 h (black), 1 h (light red) and 2 h (red). The substrate concentration of the batch reaction was 5 mM ATP, and the solution volumes used for 1 h and 2 h were 1.2 and 2.4 mL, respectively (calculated from the flux in the flow mode at the same time). EAGs were recovered by centrifugation and washed twice with 1 mL of PBK buffer. (b) Determination of the amount of enzyme shed in in the reaction solution and scrubbing solution during the recovery of EAGs. The calculation of detachment rate was based on 5 mg EAG. (c) The detachment and inactivation of EAG after 1 h and 2 h of use for batch reaction. The total loss rate was calculated according to the conversion rate of 10 min in the activity test. The inactivation rate of EAG reached 2.3% and 5.8% after batch reaction of 1 h and 2 h, respectively.
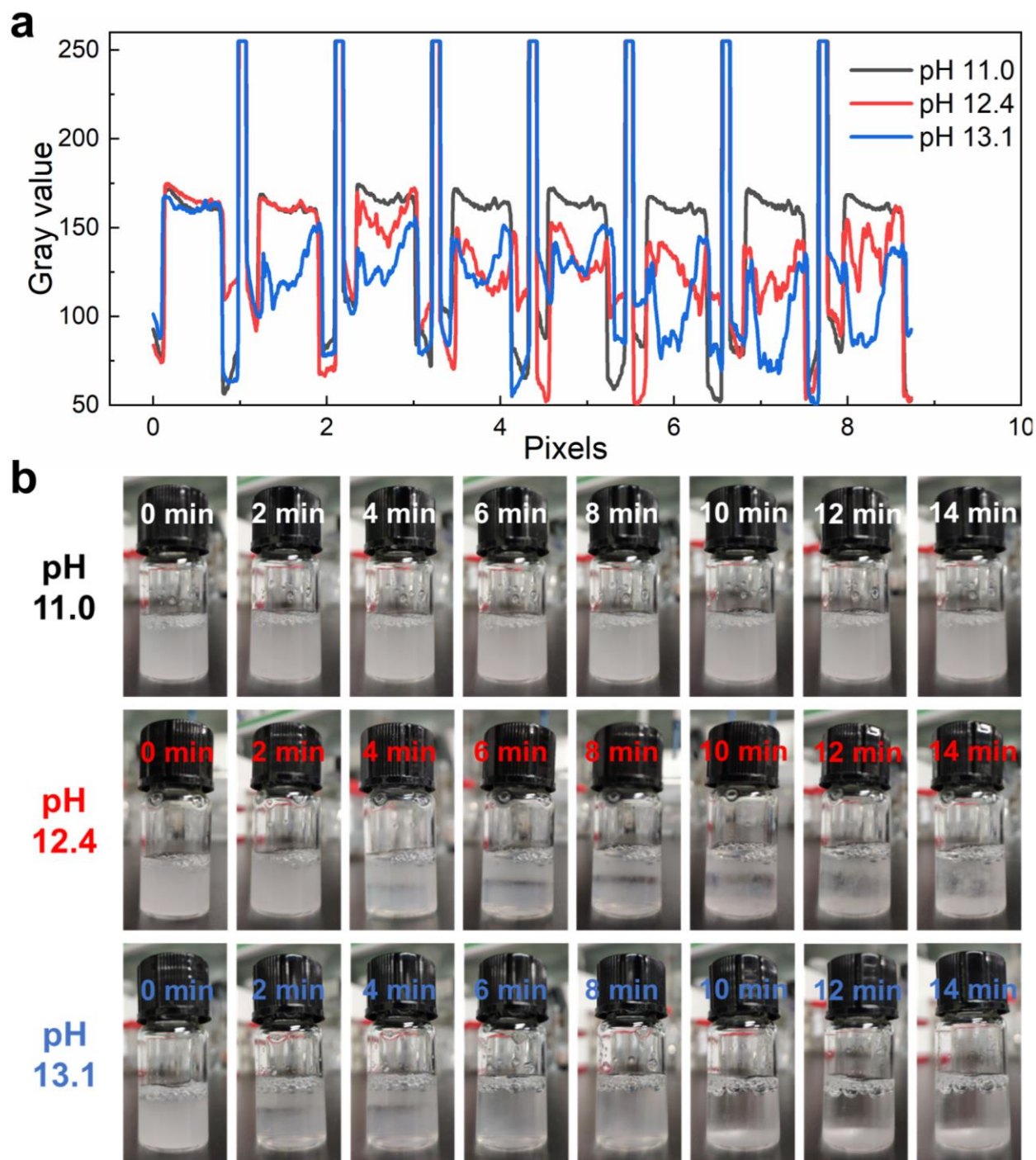
Figure S14. Stability test of EAGs in high pH solutions. (a) Variation of gray value of solution in glass bottle at different pH. One cycle for pixels corresponds to a time of 2 min. Under the condition of pH 11.0, the gray value of each cycle remains stable. However, at pH 12.4 and 13.1, the gray value becomes unstable with the increase of the period, and gradually decays. (b) Optical photographs of the dissolution of EAGs over time under different pH conditions.
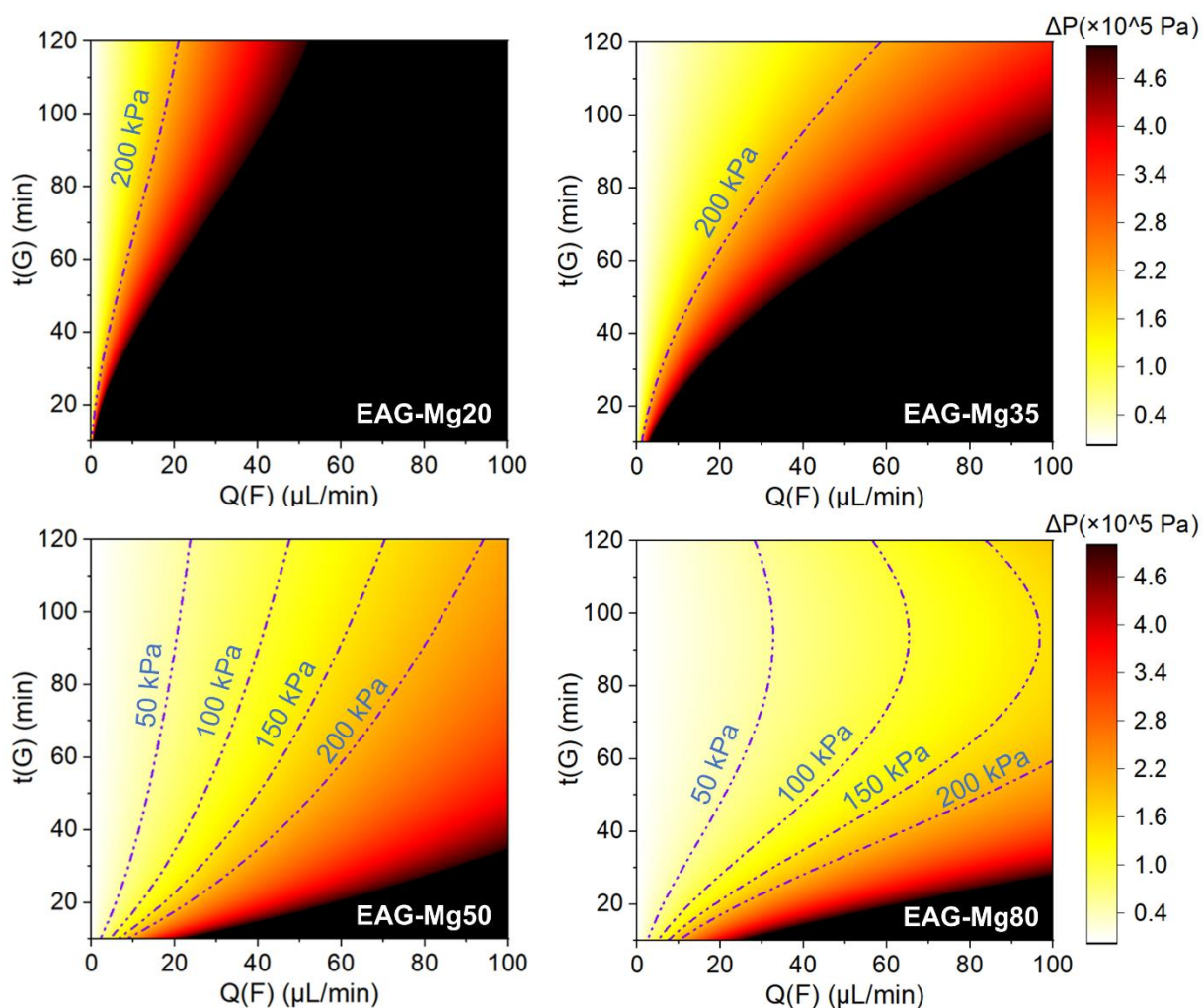
Figure S15. Numerical prediction of pressure drop in MC-MCR under the combined influence of gelation time t(G) and operating flowrate Q(F) at different c(Mg^{2+}); see Supplementary Note 1.
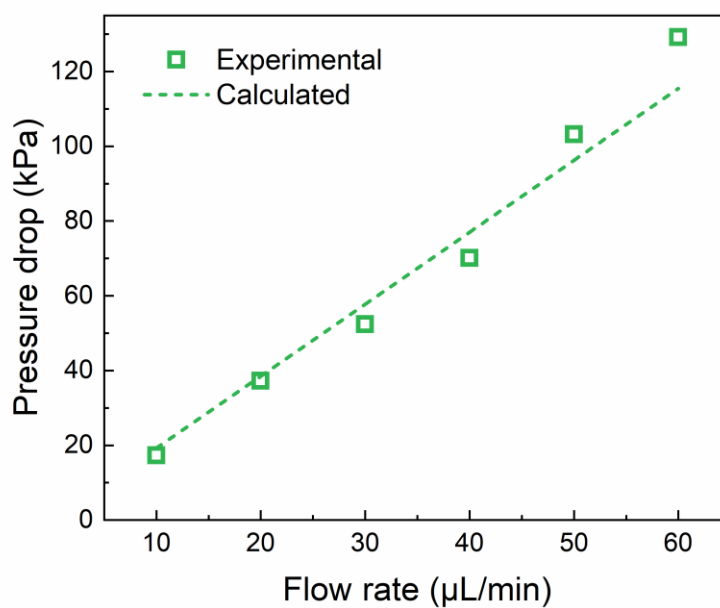
Figure S16. Comparison of experimental and calculated values of pressure drop in MC-MCR as a function of Q(F). The c(Mg^{2+}) was 50 mM, and t(G) was 120 min.
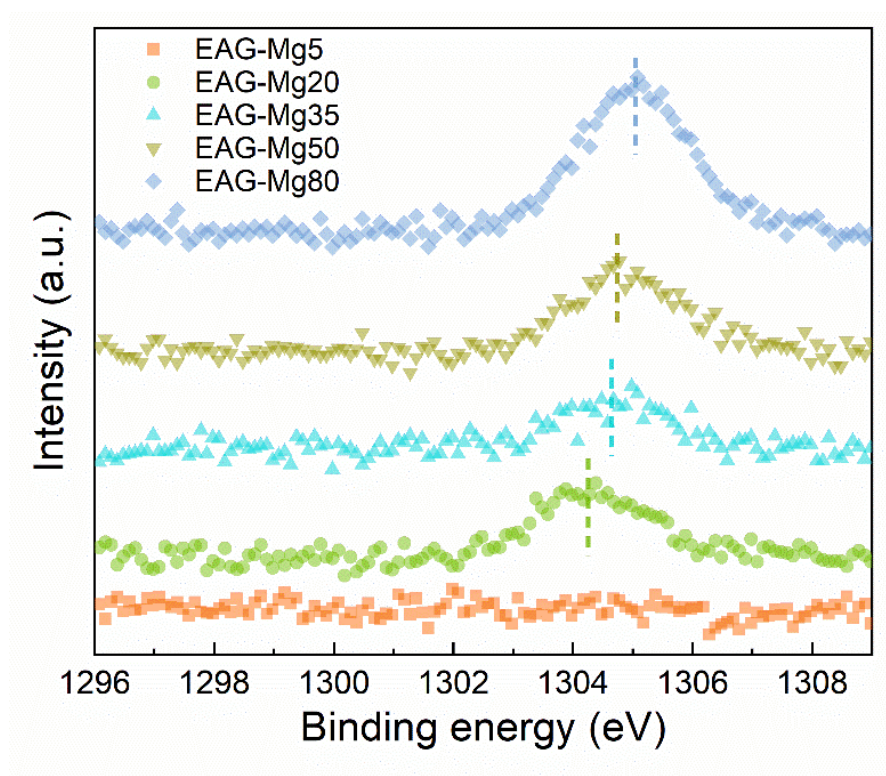
Figure S17. High-resolution Mg 1s XPS spectra of EAGs synthesized with different Mg^{2+} concentrations. For 5 mM Mg^{2+} concentration, too low Mg content in the synthesized EAG resulted in insignificant XPS signal. The peak signal of Mg 1s gradually increased with increasing Mg concentration, implying increased Mg content in EAG. Moreover, the increase of Mg^{2+} concentration led to the increase of binding energy, indicating that there were more Mg^{2+} with low coordination number of chelation in EAG synthesized with high Mg^{2+} concentration, which may be due to the increased competition between Mg^{2+}.

Figure S18. Chromatographs of standards racemic mixture of *R*-**2a** and *S*-**2a**, and the products from the assymetric resuction of **1a** catalyzed by EAG.

Figure S19. Chromatographs of standards racemic mixture of *R*-**2b** and *S*-**2b**, and the products from the assymetric resuction of **1b** catalyzed by EAG.

Figure S20. Chromatographs of standards racemic mixture of *R*-**2c** and *S*-**2c**, and the products from the assymetric resuction of **1c** catalyzed by EAG.

Figure S21. Chromatographs of standards racemic mixture of *R*-**2d** and *S*-**2d**, and the products from the assymetric resuction of **1d** catalyzed by EAG.
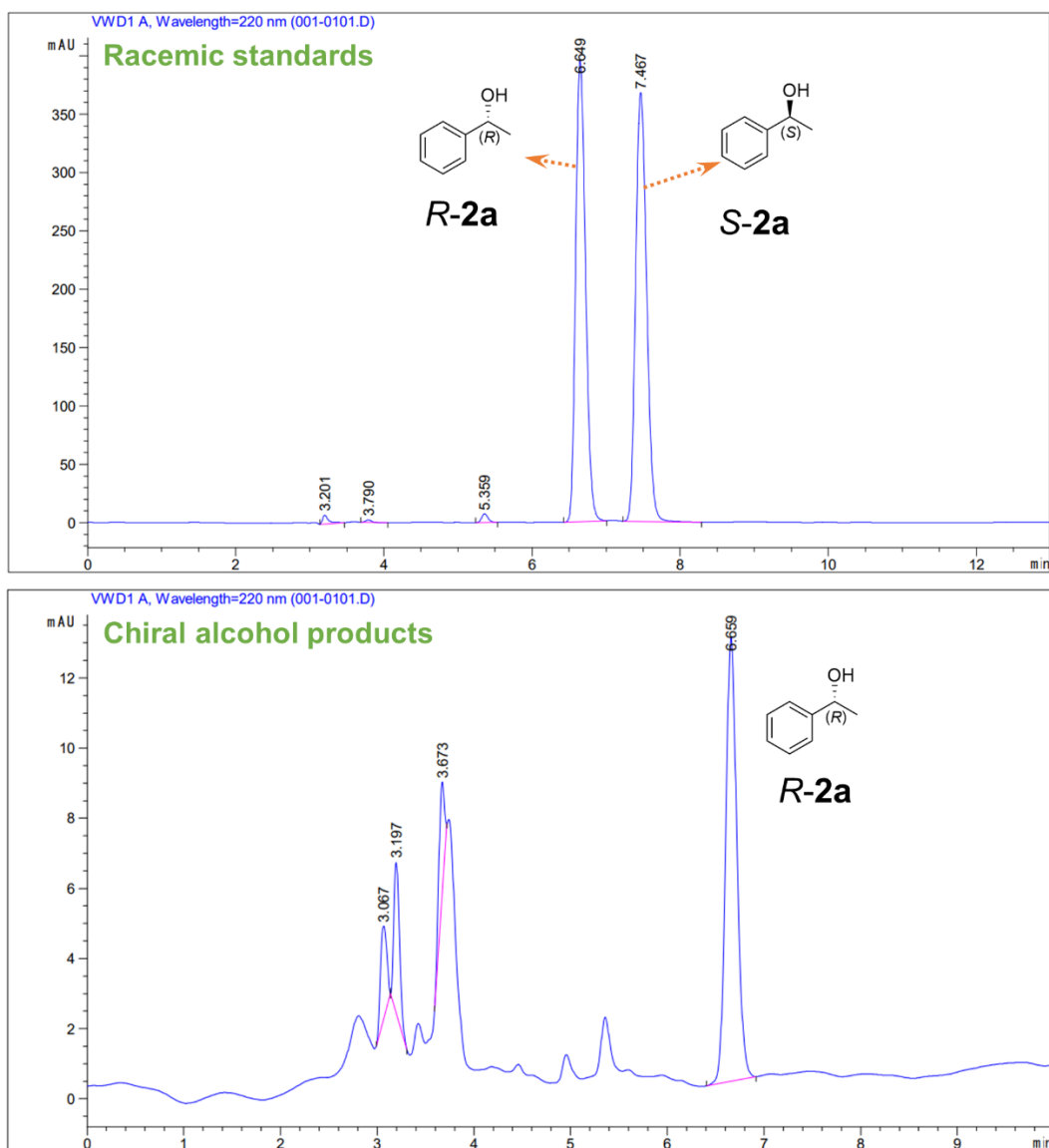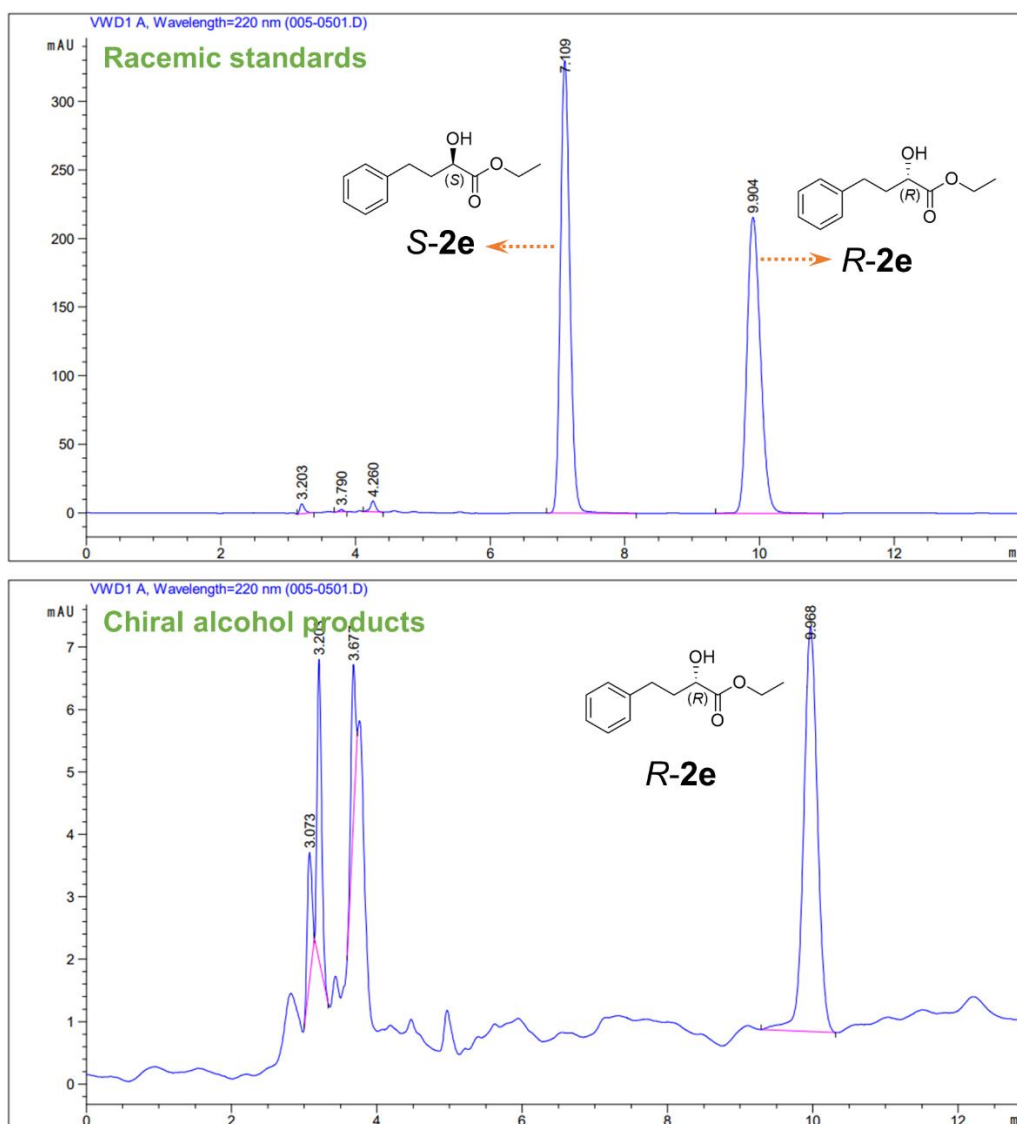
Figure S22. Chromatographs of standards racemic mixture of *R*-**2e** and *S*-**2e**, and the products from the assymetric resuction of **1e** catalyzed by EAG.
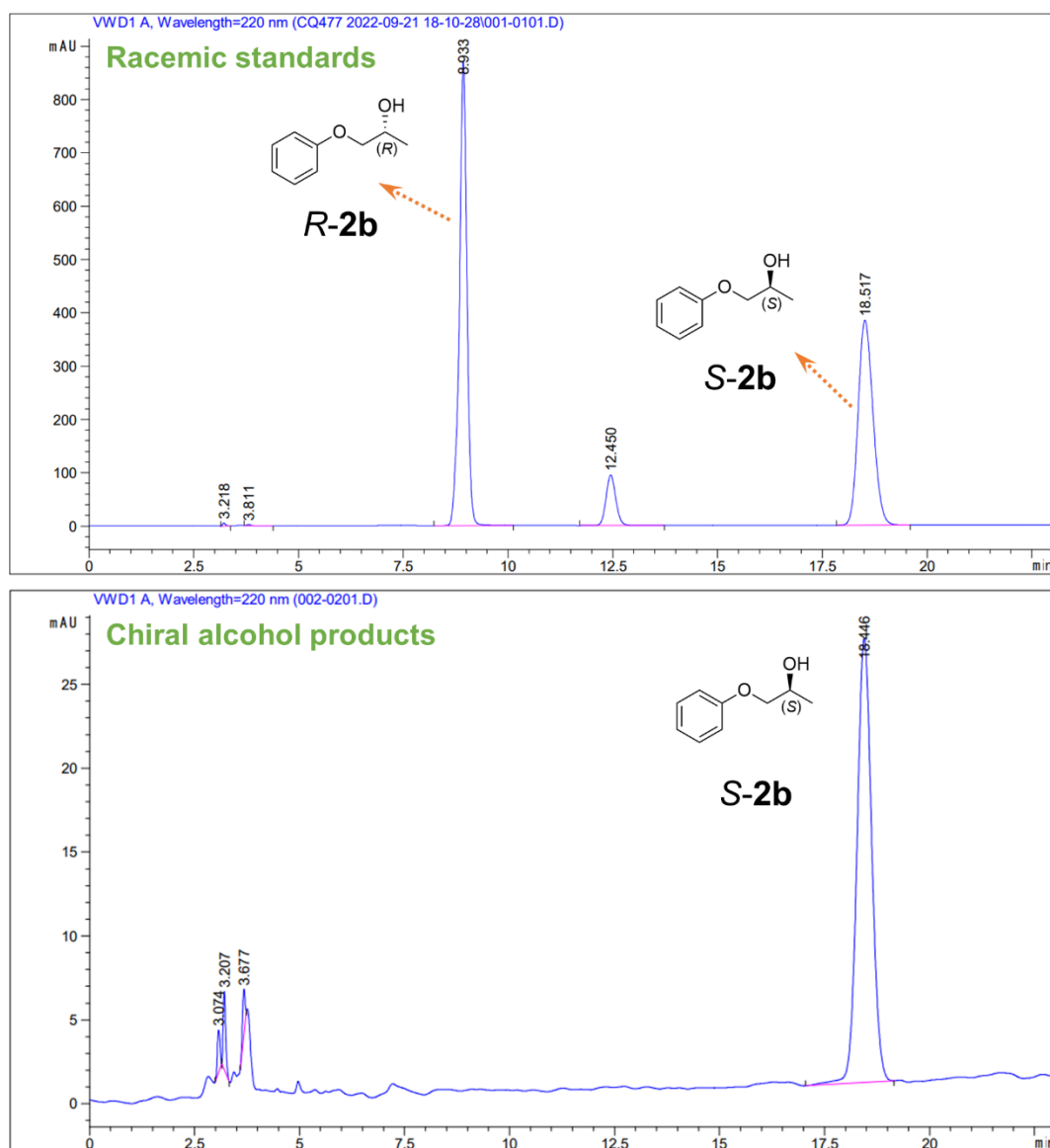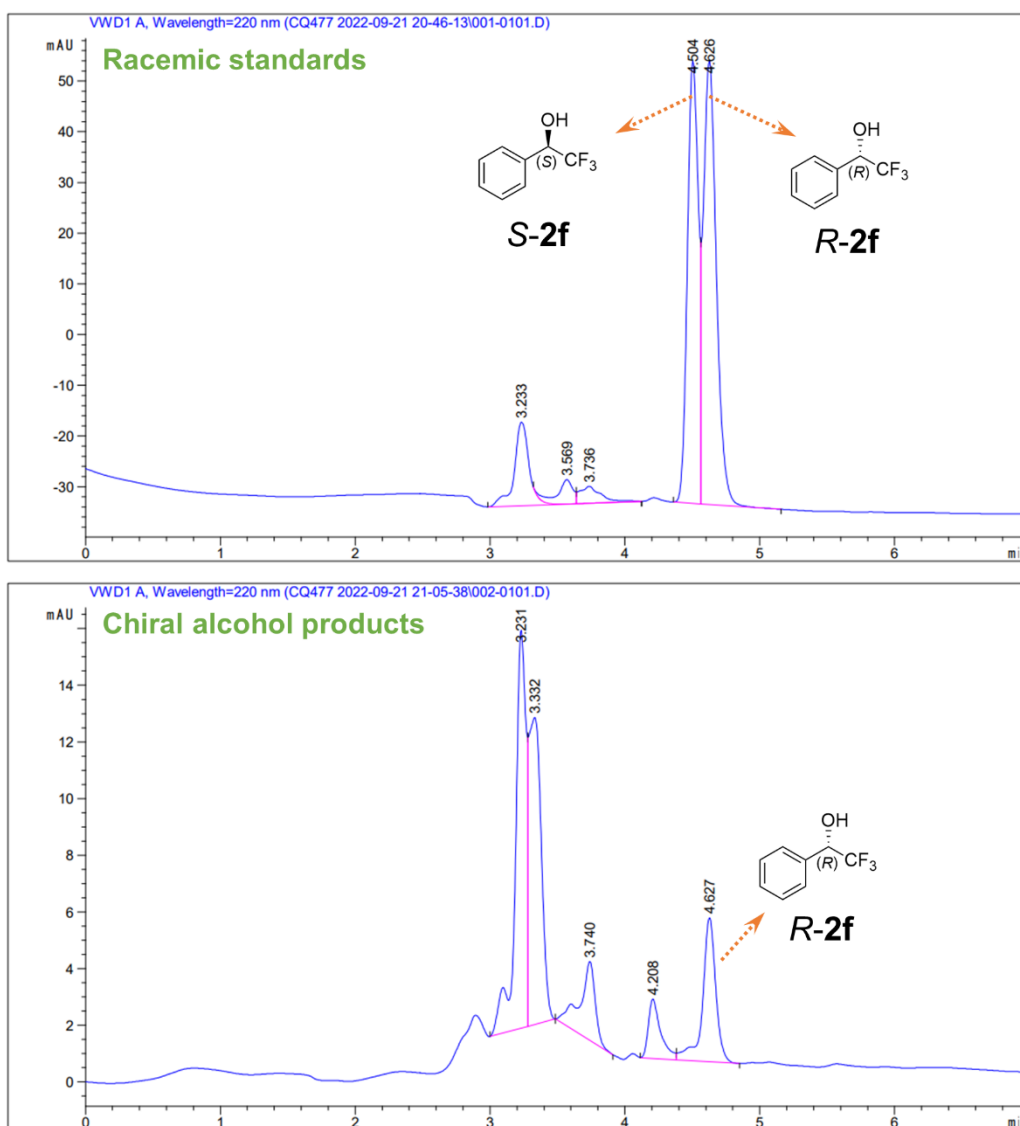
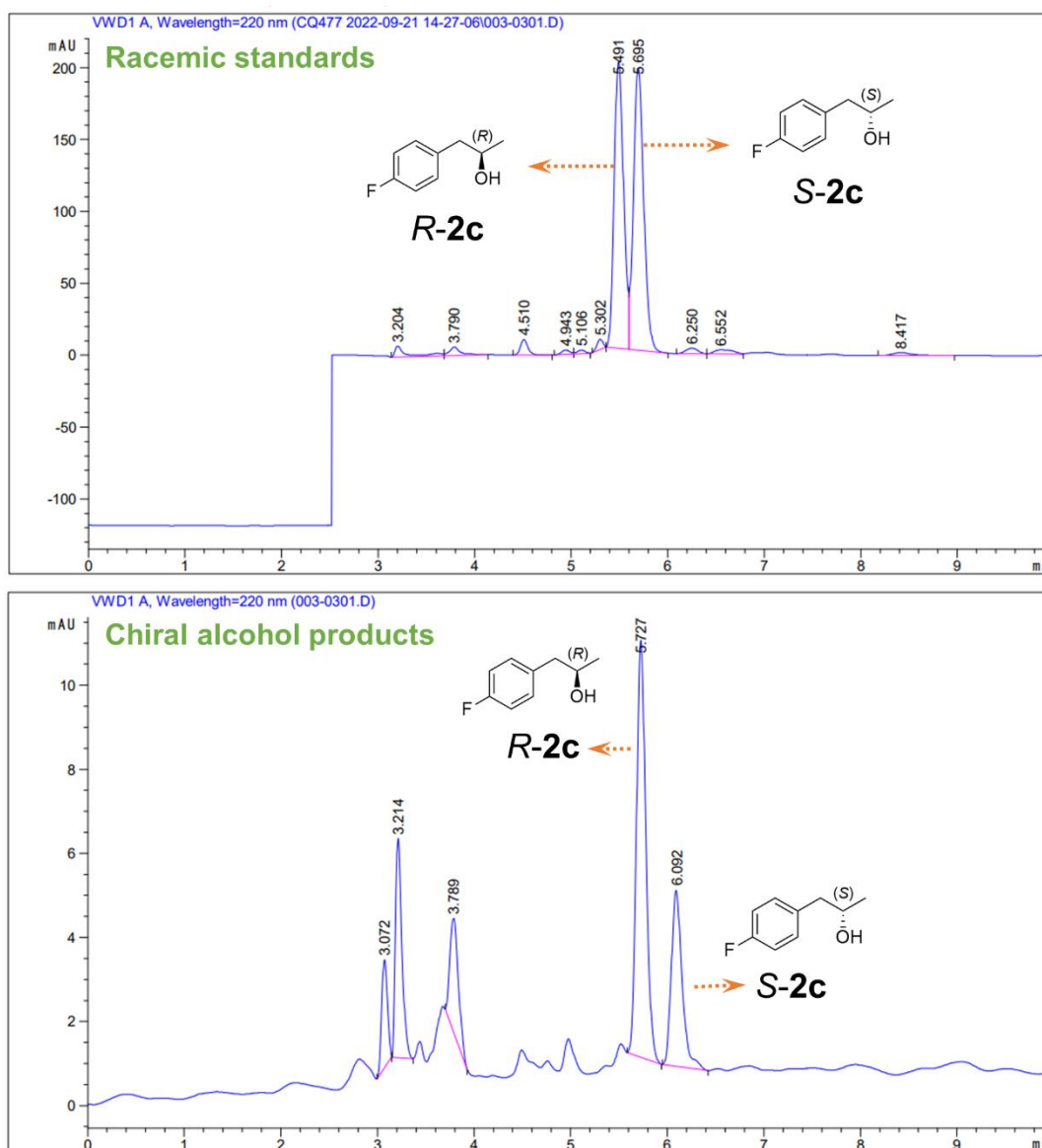**Figure S23.** Chromatographs of standards racemic mixture of *R*-**2f** and *S*-**2f**, and the products from the assymetric resuction of **1f** catalyzed by EAG.
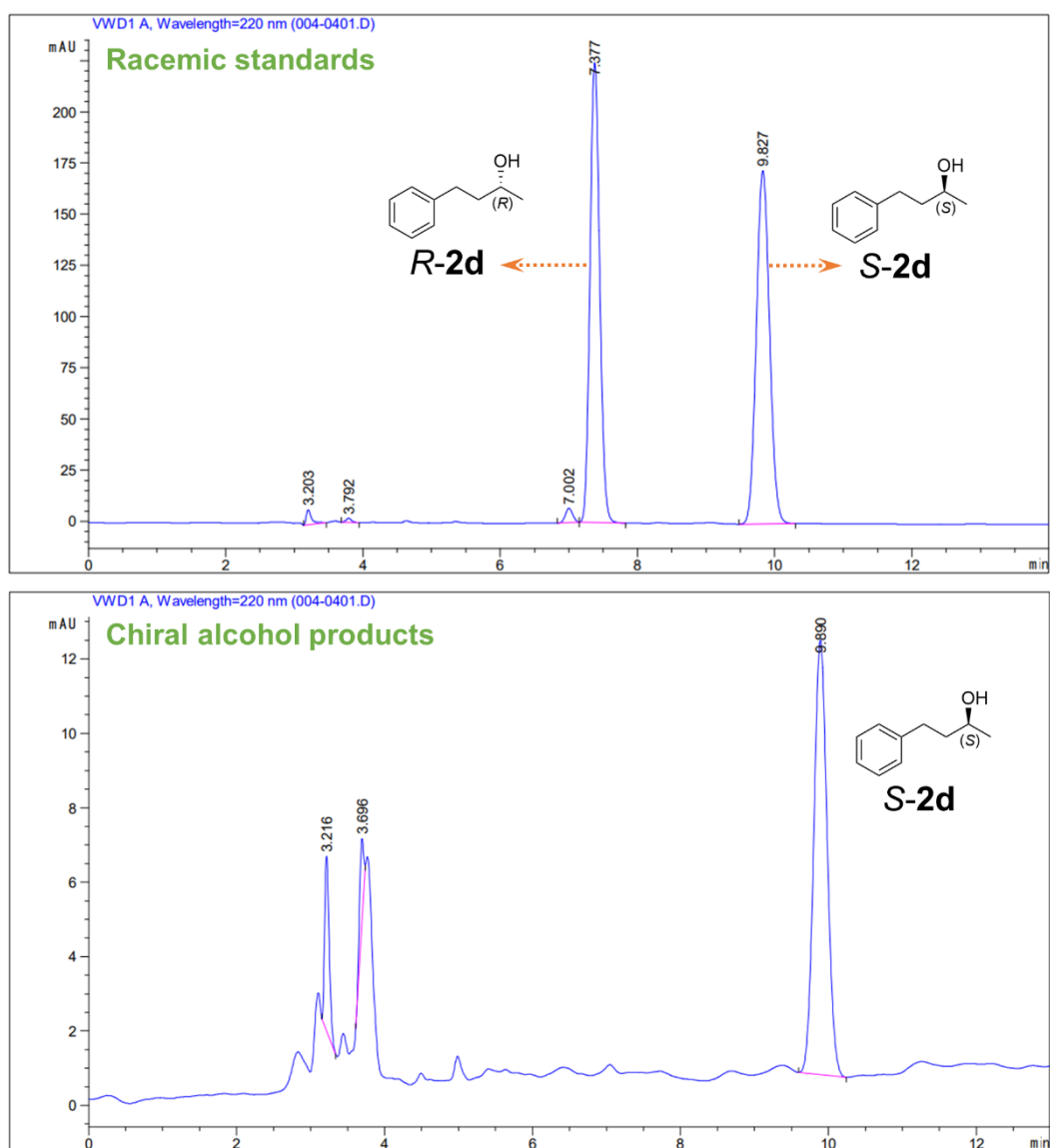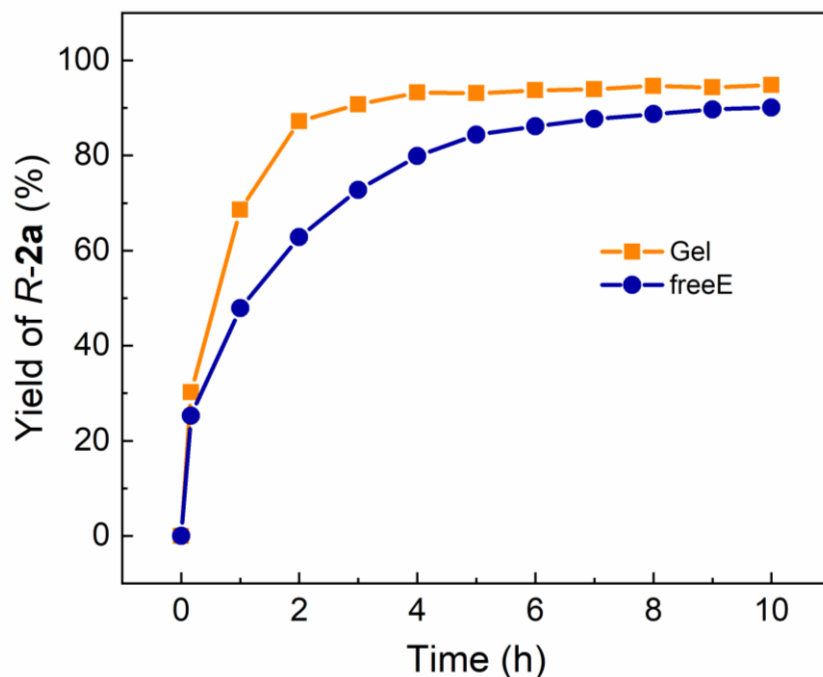
Figure S24. Variation of *R*-**2a** yields catalyzed by freeE and Gel over time in batch reaction mode. For Gel and freeE, the time required to reach 90% yield was about 3 h and 10 h of batch reactions, respectively. For the flow mode involving Gel, a residence time of 2 min was required to achieve over 90% yield of the outlet product. The calculations of STY in Figure 5c were based on yields above 90%. STY (flow) = Substrate concentration (mmol/μL) × yield (%)/100 × flow (μL/min) ×M. weight (product, mg/mmol) × 60 (min/h) / reactor volume (mL). STY (batch) = Substrate concentration (mmol/μL) × yield (%)/100 ×M. weight (product, mg/mmol) × 10^{-3} (μL/mL) / reaction time (h). The calculations were referenced in the literature.[5]

Supplementary Tables

Table S1. Summarization of methods used for continuous flow reduction of acetophenone to chiral alcohols in literatures.

Entry	Supports	Methods	Operation	STY[a] /g L^{-1} h^{-1}	Conv.[c] /%	Ref.
1	HaloLink beads	Attachment of HaloTag ADH to HaloLink support surface	Labeling of ADH, Labeling of surpport, coordination connection, and manual loading	43.1	80	6
2	PS-DVB-SILLPs	ADH adsorption on beads with ionic liquids and polymers	Surface modification by ionic liquid, modification by polymers, enzyme adsorption, and manual loading	11.9	51	7
3	HaloLink resin	Attachment of HaloTag ADH to HaloLink resin	Labeling of ADH, Labeling of resin, coordination connection, and manual loading	28.3[b]	90	8
4	Carbon nanotubes	ADH adsorption	Generation of carbon nanotube-lined quartz columns, ADH soaking adsorption	7.6[b]	30	9
5	Agarose beads	Reversible Ionic bonds	Agarose activation with diethyl aminoethyl, Connection through ionic bonds, and manual loading	4.3	80	10
6	Reactor surface	Covalent bonding on reactor surface	Surface functionalization with polydopamine layer, graft of glutaraldehyde layer, adding of	0.9	99	11

			polyethylenimine layer, and then enzyme bonding			
7	Superabsorber polymer particles	Ionic interactions	Surface modification of polymers, Ionic bonding, and manual loading	7.5	63	[12]

[a] The initial space-time yields of asymmetric reduction of acetophenone to chiral alcohols in flow reactors, where the values reported in the literature were directly used without additional calculations. [b] STY was not given directly, thus it was calculated based of the conversion in the initial stage of flow catalysis. STY = Substrate concentration (mmol/μL) × conversion (%)/100 × selectivity (%)/100 × flow (μL/min) ×M. weight (product, mg/mmol) × 60 (min/h) / reactor volume (mL). [c] The conversion rate corresponding to the STY value.

Table S2. Results of polynomial fitting parameters for EAG growth curves at different magnesium ion concentrations. Units: t(G), min; d, nm.

$C_{Mg^{2+}}$ /mM	Fitting coefficient of DLS growth $d = C_0 + C_1 t(G)^1 + C_2 t(G)^2 + C_3 t(G)^3$				-ΔP
	C_0	C_1	C_2	C_3	
20	-90.699	36.901	-0.116	0	
35	245.390	39.763	-0.039	0	$f(d, Q)$
50	614.201	92.474	-0.517	0.001	
80	626.393	127.790	-0.680	0	

Table S3. Continuous flow asymmetric reduction of 50 mM **1a** at different flow rates.

Entry	Flow (μL/min)	$t_{residence}$ (min)[a]	Conversion (%)[b]	ee (%)[c]	Productivity (mg/h)[d]
1	2	20	97.6	99	0.86
2	5	8	95.7	99	2.10

33

3	10	4	93.8	99	4.13
4	20	2	90.1	99	7.92
5	50	0.8	75.5	99	16.59
6	100	0.4	66.6	99	29.30
7	200	0.2	42.6	99	37.47

[a] Residence time in the microreactor = reactor volume (µL)/flow (µL/min). Reactor volume = 90 µL. [b] Conversion values were calculated by HPLC of the reaction solution. [c] ee values were calculated by chiral HPLC and here referred to the R-: S- chiral alcohol. [d] Productivity = concentration (mmol/µL) × conversion (%)/100× selectivity (%)/100 × flow (µL/min) ×M. weight (product, mg/mmol) × 60 (min/h).

Table S4. Source data and calculations for the STY and TTN from the cited literatures in Figure 5d.

Ref.	Substrate /mM	Average yield [a] /%	Running time /h	Flow /µL min^{-1}	Reactor volume /µL	Enzyme [c] /mg	Average STY [f] /g L^{-1} h^{-1}	TTN [g] /10^4
R47							11.85 [b]	11.9 [b]
R48	100	48	8	3.33	200	1	7.5 [b]	1.08
R49	50	90	72	30	350	4	28.3	20.6
R50							1.25 [b]	250 [b]
R51	8.7	30		25	63		7.6	2.4 [b]
R52							0.15 [d]	0.85 [d]
R53	10	55	1.5	132	288	5	18.5	0.18
R54							0.7 [b]	16 [d]
R55	50	37	2	8.33	500	0.32	2.26	0.81
R56							4.3 [b]	2 [b]
R57							15.4 [b]	0.79 [b]
R58	-	75	15	67.7	1.07×10^6	36 [e]	0.02 [d]	0.78
R59	5	92	110	50	251	3.45	6.7	6.2
R60							2.3 [d]	0.27 [d]
R61							43.1 [b]	1.6 [e]

| This work | 50 | 75 | 100 | 20 | 80 | 10 | 68.2 | 6.26 |

[a] The average yield was calculated by simplifying the conversion rate into linear attenuation during the corresponding running time. [b] Values given directly in the literature, where requires no calculation. [c] The molecular weight of alcohol dehydrogenase adopted 141 kDa. [d] Obtained by transforming the existing data in the literature. [e] Estimated value based on experience. [f] Average STY = Substrate concentration (mmol/µL) × average yield (%)/100 × flow (µL/min) ×M. weight (product, mg/mmol) × 60 (min/h) / reactor volume (mL). [g] TTN = Substrate concentration (mmol/µL) × average yield (%)/100 × flow (µL/min) × running time (h) ×M. weight (enzyme, mg/mmol) × 60 (min/h) / enzyme amount (mg).

Table S5. Zn $2p_{3/2}$, Zn $2p_{1/2}$ values for Zn species: full width at half maxima (FWHM, eV) and doublet separation values (eV).

Sample	Zn $2p_{3/2}$ (eV)	Zn $2p_{1/2}$ (eV)	Doublet separation (eV)	FWHM of Zn $2p_{3/2}$ (eV)	FWHM of Zn $2p_{1/2}$ (eV)
Metal Zn(0) [a]	1021.65	1044.66	23.01	0.86	1.04
EAG-Mg5	1021.60	1044.66	23.06	1.76	1.24
EAG-Mg20	1021.68	1044.78	23.10	1.79	1.19
EAG-Mg35	1021.82	1044.92	23.10	1.70	1.17
EAG-Mg50	1021.92	1045.11	23.19	2.02	1.22
EAG-Mg80	1022.14	1045.36	23.22	1.99	1.16

[a] Reported values from reference.[13] FWHM values of Zn $2p_{3/2}$ or Zn $2p_{1/2}$ for all Mg concentrations are greater than that of the metal, and the FWHM of Zn $2p_{3/2}$ are greater than FWHM of Zn $2p_{1/2}$. Thus, Zn 2p can be assigned as oxide peaks for the analysis of the shifting in oxidation state. The results in Table S5 demonstrated that the characteristic doublet peaks of Zn 2p shifted to high binding energy with the increase of Mg^{2+} concentration, which may be due to the change of the coordination bond length between Zn and amino acid residues caused by the incorporation of Mg^{2+}.[14] It is suggested that the excessively high Mg^{2+} concentration induced a greater change in the structure of the protein's active center, resulting in a decrease in catalytic activity.

Table S6. Conditions for chiral HPLC analyses.

Entry	Alcohol	Procedure	Retention time
1	*R*-**1a**	*n*-hexane: isopropanol=92%: 8% (v/v),	*R*-**1a**: 6.6 min
	S-**1a**	1 mL/min, 30 °C, 220nm,	*S*-**1a**: 7.5 min
		OD-H column (4.6 mm × 250 mm, 5 μm, Diacel)	
2	*R*-**1b**	*n*-hexane: isopropanol=92%: 8% (v/v),	*R*-**1b**: 8.9 min
	S-**1b**	1 mL/min, 30 °C, 220nm,	*S*-**1b**: 18.5 min
		OD-H column (4.6 mm × 250 mm, 5 μm, Diacel)	
3	*R*-**1c**	*n*-hexane: isopropanol=92%: 8% (v/v),	*R*-**1c**: 5.5 min
	S-**1c**	1 mL/min, 30 °C, 220nm,	*S*-**1c**: 5.7 min
		OD-H column (4.6 mm × 250 mm, 5 μm, Diacel)	
4	*R*-**1d**	*n*-hexane: isopropanol=92%: 8% (v/v),	*R*-**1d**: 7.4 min
	S-**1d**	1 mL/min, 30 °C, 220nm,	*S*-**1d**: 9.8 min
		OD-H column (4.6 mm × 250 mm, 5 μm, Diacel)	
5	*R*-**1e**	*n*-hexane: isopropanol=92%: 8% (v/v),	*S*-**1e**: 7.1 min
	S-**1e**	1 mL/min, 30 °C, 220nm,	*R*-**1e**: 9.9 min
		OD-H column (4.6 mm × 250 mm, 5 μm, Diacel)	
6	*R*-**1f**	*n*-hexane: isopropanol=75%: 25% (v/v),	*S*-**1f**: 4.5 min
	S-**1f**	1 mL/min, 30 °C, 220nm,	*R*-**1f**: 4.6 min
		OD-H column (4.6 mm × 250 mm, 5 μm, Diacel)	

Supplementary Note

Supplementary Note 1. Pressure drop calculation for the monolithic microchannel.

The Ergun equation[15] is widely used in the prediction and analysis of frictional resistance of flow in a packed bed, and the equation is as follows:

$$-\frac{\Delta P}{L} = \frac{150(1-\varepsilon)^2}{d^2\varepsilon^3}\mu J + \frac{7(1-\varepsilon)}{4d\varepsilon^3}\rho J^2$$

Where ΔP is the pressure drop. L is the length of the porous medium channel. ρ and μ are the density and dynamic viscosity of the fluid, respectively. 150 and 7/4 are empirical constants based on experiments, respectively. ε is the porosity of the porous medium. d is the effective diameter of the particles that make up the porous medium. J appears to be the apparent velocity of the fluid within the porous medium.

For the flow range (<200 μL/min) used in this work, the calculated Re_ε is far below 10, which belongs to laminar flow. Therefore, the pressure-drop due to inertial force, the second term in Ergun's equation, can be ignored. Therefore, the pressure-drop prediction model can be simplified to the Blake-Kozeny equation[16] as follows:

$$-\frac{\Delta P}{L} = \frac{150(1-\varepsilon)^2}{d^2\varepsilon^3}\mu J$$

The apparent flow velocity can be calculated according to the flow Q and the microchannel cross-sectional area S, so the pressure prediction model can be calculated according to the following formula:

$$-\Delta P = \frac{150(1-\varepsilon)^2\mu L}{\varepsilon^3 S}\cdot\frac{Q}{d^2}$$

Therefore, the pressure drop can be predicted based on the operating flow Q and the effective diameter d when the EAG enters the microchannel chip. The change of the EAG diameter with the gelation time t_G has been measured by DLS (Figure S10), and the relationship between d and t_G can be obtained by fitting the growth curve, as shown in Table S2. Thus, the predictive model of pressure drops for the EAG monolithic microchannel can be obtained as follows:

$$(-\Delta P)_{\text{EAG-Mg20}} = \frac{150(1-\varepsilon)^2\mu L}{\varepsilon^3 S}\cdot\frac{Q}{[-90.699 + 36.901t(G) - 0.116t(G)^2]^2}$$

$$(-\Delta P)_{\text{EAG-Mg35}} = \frac{150(1-\varepsilon)^2\mu L}{\varepsilon^3 S}\cdot\frac{Q}{[245.39 + 39.763t(G) - 0.039t(G)^2]^2}$$

$$(-\Delta P)_{\text{EAG-Mg50}} = \frac{150(1-\varepsilon)^2\mu L}{\varepsilon^3 S}\cdot\frac{Q}{[614.201 + 92.474t(G) - 0.517t(G)^2 + 0.001t(G)^3]^2}$$

$$(-\Delta P)_{\text{EAG}-\text{Mg80}} = \frac{150(1-\varepsilon)^2\mu L}{\varepsilon^3 S} \cdot \frac{Q}{[626.393 + 127.79t(G) - 0.68t(G)^2]^2}$$

The difference in pressure drop in SC-MCR and MC-MCR at low *Re* is derived from the length *L*, cross-sectional area *S*, and the porosity ε of EAG monolith. As shown in Figure 4d, the EAG monolith in MC-MCR had a larger average pore size (0.66 *vs* 0.43 μm), and its porosity was about 1.24 times higher than that in SC-MCR. Meanwhile, according to that the length and cross-sectional area of MC-MCR were 1.6 and 0.63 times that of SC-MCR respectively, it can be calculated that the pressure drop in MC-MCR was about 1.08 times that in SC-MCR.

References

1. G. Qu, Y. Bi, B. Liu, J. Li, X. Han, W. Liu, Y. Jiang, Z. Qin and Z. Sun, *Angew. Chem., Int. Ed.*, 2021, DOI: 10.1002/anie.202110793.
2. Z. T. Sun, G. Y. Li, A. Ilie and M. T. Reetz, *Tetrahedron Lett.*, 2016, **57**, 3648-3651.
3. Z. T. Sun, R. Lonsdale, A. Ilie, G. Y. Li, J. H. Zhou and M. T. Reetz, *Acs Catal.*, 2016, **6**, 1598-1605.
4. X. Y. Li, Y. F. Cao, K. Luo, Y. Z. Sun, J. R. Xiong, L. C. Wang, Z. Liu, J. Li, J. Y. Ma, J. Ge, H. Xiao and R. N. Zare, *Nat. Catal.*, 2019, **2**, 718-725.
5. R. Porcar, V. Sans, N. Rios-Lombardia, V. Gotor-Fernandez, V. Gotor, M. I. Burguete, E. Garcia-Verdugo and S. V. Luis, *Acs Catal.*, 2012, **2**, 1976-1983.
6. B. Baumer, T. Classen, M. Pohl and J. Pietruszka, *Adv. Synth. Catal.*, 2020, **362**, 2894-2901.
7. R. Porcar, I. Lavandera, P. Lozano, B. Altava, S. V. Luis, V. Gotor-Fernandez and E. Garcia-Verdugo, *Green Chem.*, 2021, **23**, 5609-5617.
8. J. Dobber, M. Pohl, S. V. Ley and B. Musio, *React. Chem. Eng.*, 2018, **3**, 8-12.
9. C. Zor, H. A. Reeve, J. Quinson, L. A. Thompson, T. H. Lonsdale, F. Dillon, N. Grobert and K. A. Vincent, *Chem. Commun.*, 2017, **53**, 9839-9841.
10. A. I. Benitez-Mateos, E. San Sebastian, N. Rios-Lombardia, F. Moris, J. Gonzalez-Sabin and F. Lopez-Gallego, *Chem.-Eur. J.*, 2017, **23**, 16843-16852.
11. K. T. Sriwong and T. Matsuda, *React. Chem. Eng.*, 2022, **7**, 1053-1060.
12. N. Adebar and H. Groeger, *Bioengineering-Basel*, 2019, **6**, 99.
13. M. C. Biesinger, L. W. M. Lau, A. R. Gerson and R. S. C. Smart, *Appl. Surf. Sci.*, 2010, **257**, 887-898.
14. M. Claros, M. Setka, Y. P. Jimenez and S. Vallejos, *Nanomaterials*, 2020, **10**. DOI: 10.3390/nano10030471.
15. S. Ergun, *Chem. Eng. Prog.*, 1952, **48**, 89-94.
16. M. J. Macdonald, C. F. Chu, P. P. Guilloit and K. M. Ng, *AIChE J.*, 1991, **37**, 1583-1588.